in-situ Transmission Electron Microscopy of Collagen

Schoffelen, T.

Award date:
2020

MSc. Thesis

in-situ Transmission Electron Microscopy of Collagen

Tom Schoffelen
0883875

11 February 2020

Supervising professor:
Prof. dr. G. de With

Supervisor:
H. Wu

Graduation Committee:
Prof. dr. G. de With
H. Wu
Dr. H. Friedrich
Dr. S. Hoffman Boss

EINDHOVEN UNIVERSITY OF TECHNOLOGY

Department of Chemical Engineering and Chemistry

Physical Chemistry - SPC

Building Helix
Het Kranenveld 14
P.O. Box 513
5600 MB Eindhoven

www.chem.tue.nl

Preface

Understanding the smallest building blocks of life is a fascinating journey that requires the use of state-of-the-art equipment, cooperating with the brightest minds, and developing new ideas along the way. It is a privilege to work in this field.

Summary

Collagen, the most abundant protein in bone, tendon, skin, and muscles, is characterized by its hierarchical structure and fascinating mechanical properties. It plays a paramount role in many structural components of the human body. Collagen fibrils are an intermediate building block in the hierarchical structure and contain a large amount of tropocollagen molecules aligned in a specific quasi-hexagonal pattern. An important feature of this pattern is *D*-band spacing, which is attributed to a periodic occurrence of overlap and gap zone between adjacent molecules. In nature, collagen fibrils undergo a mineralization process to attain unique structural properties. This process has been explored widely on lab scale and evidence shows that different degrees of mineralization can lead to significantly different mechanical properties.

Obtaining nanoscale information regarding both local *D*-band spacing changes and collagen mineralization requires state-of-the-art analytical techniques. *D*-band spacing change is often determined using either small angle x-ray scattering (SAXS) or atomic force microscopy (AFM), where the *D*-band spacing changes are averaged across a larger area or measured with less temporal resolution respectively. *In-situ* transmission electron microscopy (TEM) with its high spatial and temporal resolution is the ideal tool to employ for the tracking of local *D*-band spacing changes upon fibril strain, providing new insights on structural dynamics of the collagen structure. Analyzing in real time the collagen dynamics of mineralization at nanoscale is currently not possible and requires method development in the field of liquid phase TEM (LP-TEM).

Therefore, this thesis focuses on developing *in-situ* TEM techniques to study the collagen structure and dynamics in different conditions. First, the deformation behavior of single collagen fibril is monitored under tension in real time with a strong focus on changes in *D*-band spacing; second, the development of a new LP-TEM workflow to probe the collagen native structure and even the mineralization process in solution is reported.

The work is organized as follows:

- Chapter one introduces background of material and methods used.
- Chapter two addresses the structure dynamics of collagen and demonstrate that collagen deforms in-homogeneously under tension. With the use of *in-situ* TEM it is possible to track local *D*-band spacing changes and to provide evidence that these changes are not equal across the length of the fibril.
- Chapter three reports the method development towards monitoring *in-situ* collagen mineralization. The strategy how to translate the collagen mineralization process from lab scale to LP-TEM is reported. Both sample preparation and liquid deposition have been optimized, however, challenges regarding absolute contrast and beam effects remain. Furthermore, lab mineralization experiments have concluded that the process cannot be translated into the liquid cell in a straightforward manner and requires greater optimization with potential liquid phase cell re-design.
- Chapter four presents the conclusions and outlook of this work. *In-situ* TEM has provided significant evidence in the debate ongoing in the scientific community regarding the deformation mechanism of collagen. Sample preparation and liquid deposition techniques have been optimized and insights are shared. In addition, despite challenges regarding *in-situ* monitoring of the mineralization behavior remain, ways to overcome them are studied and reported.

Contents

Chapter 1 Introduction

In this chapter the theoretical background is given to highlight important characteristics, challenges, and concepts of the methods and techniques applied in this thesis. First, the important features of electron microscopy are explained followed by an in-depth overview of TEM. Finally, the collagen structures and its mineralization are discussed.

1.1 Electron microscopy

The development of the first electron microscope by Ruska in 1932 enabled accelerated insight in both nanoscience and material science. Electron microscopy gives rise to material characterization at the length scale that is far beyond the capability of an optical microscopy. According to the de Broglie relation (1), electrons that have been accelerated at high voltage hold a much smaller wavelength than visible light. In equation (1): λ is the wavelength, p the momentum, h Planck's constant, m mass, and v velocity.

$$\lambda = \frac{h}{p} = \frac{h}{mv} \tag{1}$$

Therefore, applying high energy electrons for image formation, ensures that the limit on the spatial resolution is no longer determined by the diffraction limit for visible light. Both scanning electron microscopy (SEM) and transmission electron microscopy (TEM) techniques are based on this feature; SEM and TEM microscopes generate high energy electrons in a beam which impact the specimen inside a vacuum chamber. SEM microscopes are designed primarily to work based on reflection of the electron beam to examine material surfaces, while TEM microscopes enable examination of the specimen internal-structure via transmission of the electron beam. [1] For both SEM and TEM, the interaction of electrons with the material is important to generate a signal and thus an image. Figure 1 displays the interaction of electrons with materials. Primary electrons are released from an electron source and interact with the specimen to form, amongst others, secondary electrons (SE) and back scattered electrons (BSE). [2] Concerning electron specimen interactions, there is a distinction between elastic and inelastic interactions. Elastically scattered electrons experience a change of direction but not a change of wavelength (energy); inelastic scattered electrons, on the other hand, have a longer wavelength (energy loss) and in turn generate a range of signals to characterize the material. Additionally, coherent elastically scattered electrons are used to analyze crystal structure. Important parameters influencing the inelastic scattering are specimen thickness, interaction volume, and electron transparency.

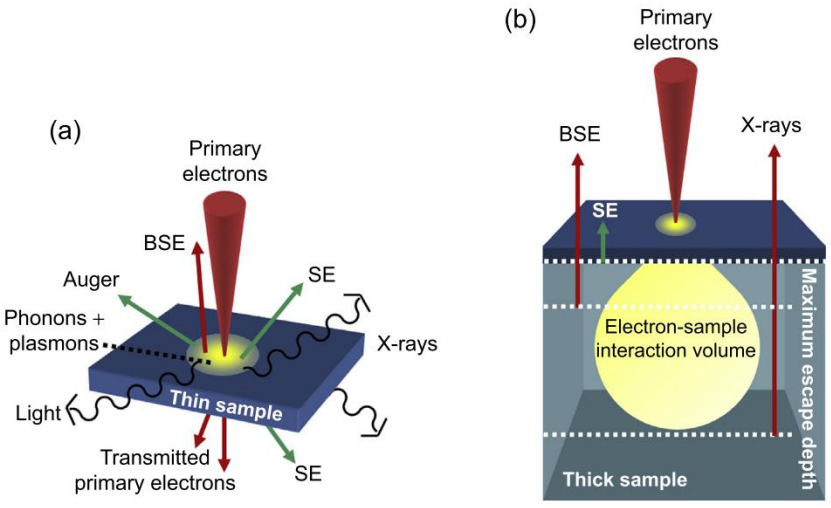

Figure 1: The interaction of incoming primary electrons with a sample. (a) Useful signals generated by electron-matter interactions in a thin sample. (b) Formation of SE, BSE, and X-rays in thick samples and limits of escape within the interaction volume. [1]

A general limitation, as part of any high-resolution imaging technique, is that only a small part of the specimen is analyzed, and additional bulk experiments are required to confirm hypothesis. Furthermore, TEM presents 2D images of 3D specimens, posing challenges in drawing conclusions on 3D scale. Additionally, ionizing radiation leads to damage of the specimen. Finally, TEM requires thin specimen, in the order of few hundred nm, and the thinning process might change both the structure and chemistry of the sample.

1.2 Transmission Electron Microscopy

TEM is a key experimental technique for visualizing and analyzing structures and morphologies of samples. [3] In order to have electrons with sufficient energy to pass through a 100 nm sample, accelerating voltages in the order of (80 to 400) keV are typically used. [2] Figure 2 illustrates the typical physical design of a TEM consisting of a series of magnetic lenses arranged sequentially along the electron beam direction. Condenser lenses before the specimen focus the electrons into a beam of controlled diameter and convergence. The objective lens focuses the transmitted electrons to form the diffraction pattern and first image. Projector lenses then magnify the image or diffraction pattern onto the detection system. For quality purposes it is critical to align several key lenses before each analysis. Specimens are placed in specifically designed holders with the possibility to tilt along one or two axes. Modern sample holders can achieve tilt angles up to 70°, relying on the physical space between the pole pieces. The ability to maneuver an object in the electron beam grants the possibility to perform 3D structure analysis by tomography. Sufficient contrast is required to distinguish objects from images obtained. The definition of contrast in quantitative terms is the difference in intensity between two adjacent areas. This difference can be obtained in several ways. Figure 3 illustrates some of the major contrast modes that involve differences in mass-density, thickness, and crystal orientation. As shown in Figure 3a, the high density region of the specimen interacts more strongly with the incoming electrons leading to a decrease in image intensity. This contrast mode is often referred to as mass-contrast and is only applicable for homogeneously thick samples. Figure 3b represents the effect of thickness difference to generate contrast. In samples with uneven thickness, TEM will provide a reduced image intensity with increasing specimen thickness, additionally providing information such as surface roughness, or object outline. The contrast effects in Figure 3a and b are generally combined as mass-thickness-contrast. This type of contrast is similar to the Lambert-Beer absorption contrast. [2] In case of crystalline structures, image contrast will also depend on the orientation of the crystal lattice with respect to the electron beam.[2] Strong diffraction spots are generated if lattice planes are parallel to the electron beam, which in turn are filtered out by the objective aperture resulting in lowered intensity, as illustrated in Figure 3c.

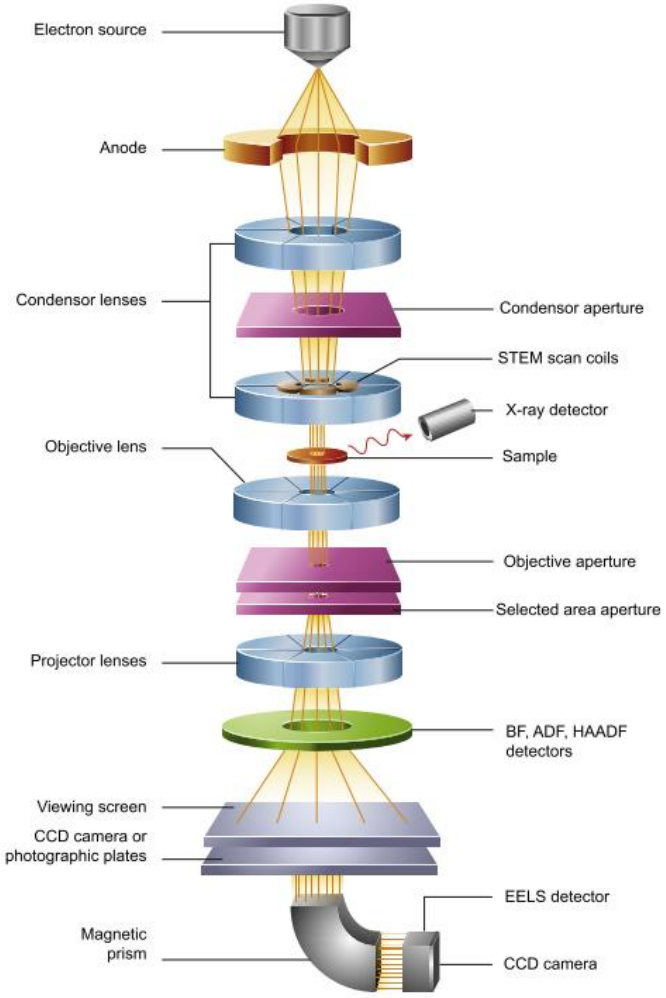

Figure 2: Schematic representation of TEM physical design. [1]

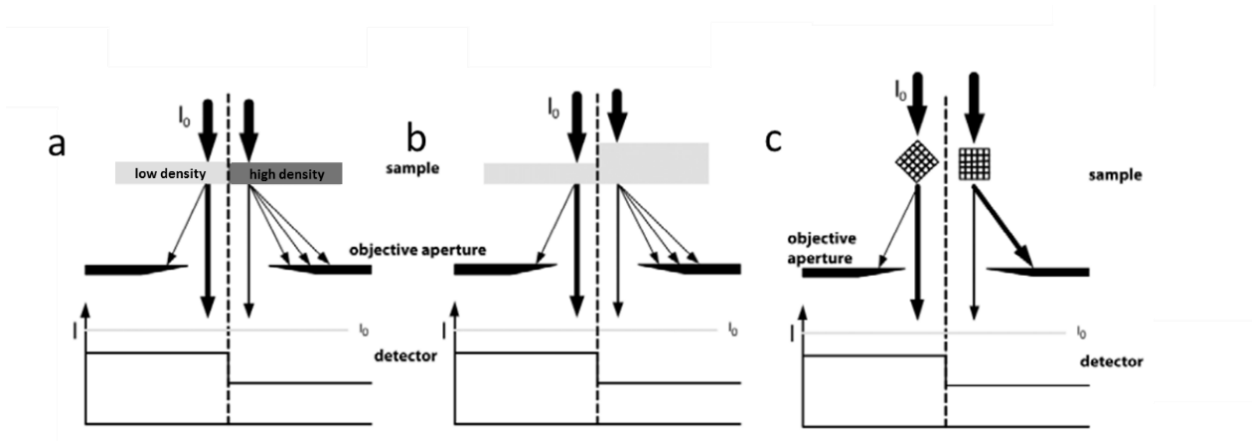

Figure 3: Schematic overview of different contrast modes. a) mass-density, b) thickness, and c) crystal orientation. [2]

Sample preparation plays a paramount role in obtaining high quality images with adequate contrast that represent the specimen without artifacts. There are several ways to prepare an electron transparent sample, amongst others ultramicrotomy, ion-beam thinning, focused ion beam (FIB) milling, and vitrification of liquid samples. Although TEM has very high resolution and is able to visualize in great detail microstructures of materials, early TEM design does not allow the availability of, for instance, heating, electrical fields, and aqueous environment to monitor processes and mechanisms. In the next chapter, the general concept of *in-situ* TEM and LP-TEM is introduced and the challenges are highlighted.

1.3 *In-situ* TEM

In-situ TEM incorporates the benefit of the high spatial and temporal resolution of the TEM with the ability to follow specimens over time with the application of external stimuli that in some cases closely reassemble real-world conditions. [4] Due to these features, a steady increase in the application of *in-situ* TEM for advanced research and the need for material scientist to further develop and optimize sample holders and sample preparations is recognized. An overview of ongoing developments, amongst others, can be found in the work of Taheri *et al.* [4], Ross [5], Tromp and Ross [6], de Jonge and Ross [7], and Cho. [8] Current available options include TEM holders that apply heat, atmospheric pressure, and even allow liquids to be present in the microscope environment. Continuous imaging of specimen allows for in-depth analysis of structural nanoscale changes.

1.3.1 LP-TEM

LP-TEM is a technique that enables direct real-time imaging of dynamic processes occurring in the presence of liquid at nanoscale. [7,9–14] With advances in microfabrication, the first liquid cell was developed by Williamson *et al*. [15] and it was based upon very thin but robust silicon nitride membranes as imaging windows. In liquid cells, a ultra-thin layer of liquid is encapsulated between a pair of microchips to ensure compatibility with the high vacuum conditions inside the electron microscope, see Figure 4.

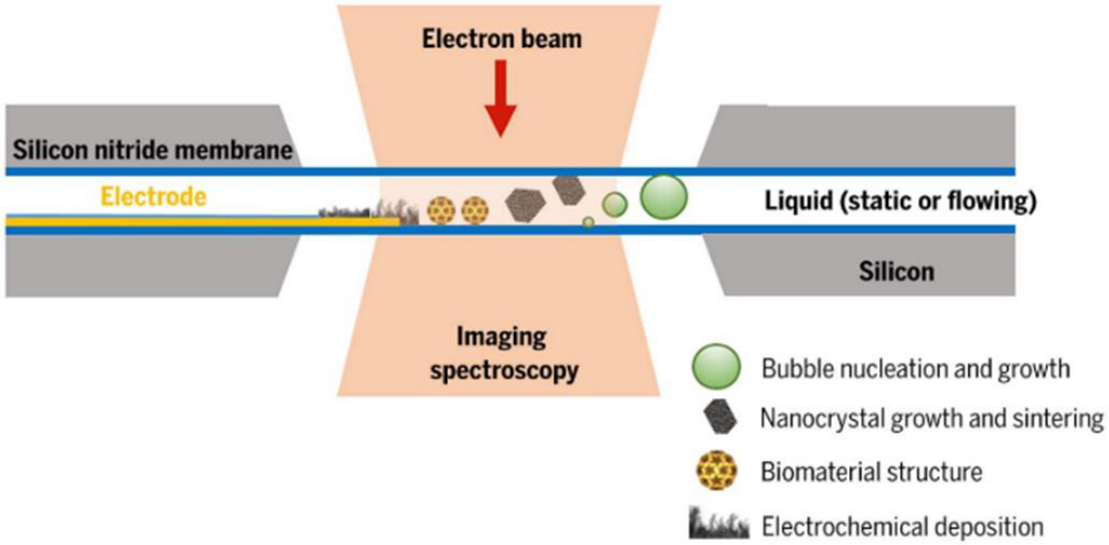

Figure 4: Liquid cell design for in-situ TEM imaging. [5]

Current state of the art silicon nitride liquid cell technology comprises dedicated TEM holders with possible additional functionalities, such as liquid flow, heating, and electrical biasing. An example of a process that can be followed by LP-TEM is liquid-liquid phase separation. [13] In order to evaluate these processes using a wider range of TEM capabilities is key and one of the main ongoing developments in the field. Developments have made it possible to apply additional microscopy modes such as dark-field, high-resolution TEM, and aberration corrected imaging. Within the field of analytical microscopy, further developments are ongoing to incorporate both electron energy-loss spectroscopy (EELS) and X-ray energy dispersive spectroscopy (XEDS) to provide chemical composition of the specimen, down to an atomic level. [5,16–18] The main limitations of liquid phase microscopy remain image resolution and electron beam effects. [5] The reduced resolution is an apparent problem related to scattering electrons in both the liquid layer as well as the window material. Liquid layer thickness is often difficult to control as window materials inherently bulge towards the center of the window due to the pressure difference between the cell interior and the high vacuum of the microscope chamber. Although there are several possibilities to control the bulging of the window and increase resolution, it has to be kept in mind that an ultra-thin layer might

generate results that are different from experiments performed in bulk. [5] Another possible route to increase resolution involves the change of the window material from silicon nitride to graphene. [5] Graphene is used to encapsulate liquid droplets. Thanks to the strong van der Waals interaction between adjacent graphene sheets, liquid pockets are formed encapsulating the sample as shown in Figure 5. In addition to the reduced thickness, graphene also assists in reducing charging of the sample. [19] The formation of closed liquid droplets eliminates the possibility to flow additional chemicals into the liquid droplet.

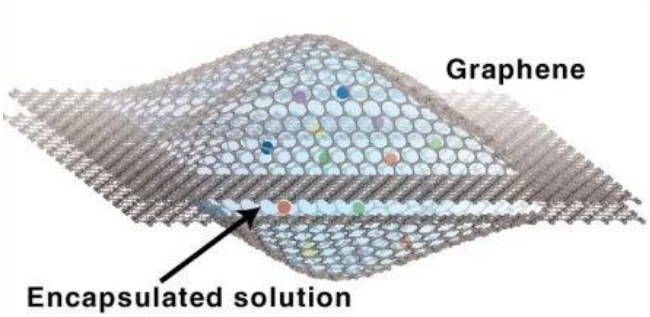

Figure 5: Schematic representation of a graphene liquid cell sample encapsulation.

While performing *in-situ* TEM, it is crucial to understand and control electron beam-induced effects which could influence the outcome of the experiment, thereby severely compromising the quality of the research and leading to wrong conclusions. [4] Beam induced effects can include: atomic displacement, sputtering, heating, ionization, and charging. [8] Transfer of the momentum of primary electrons generates displacement of atoms often referred to as knock-on damage, while surface atoms that are ejected as a result of the primary electrons lead to sputtering of the surface. Primary electrons, when scattered inelastically, can transfer their energy, causing heating, or excite the material, leading to a change in electronic configuration. Expulsion of secondary and Auger electrons results in electrostatic charging of the sample. As example, hydrated electrons from water radiolysis can cause nucleation and growth of gold nanoparticles by reducing Au(III), from $HAuCl_4$, to Au(0). [8]

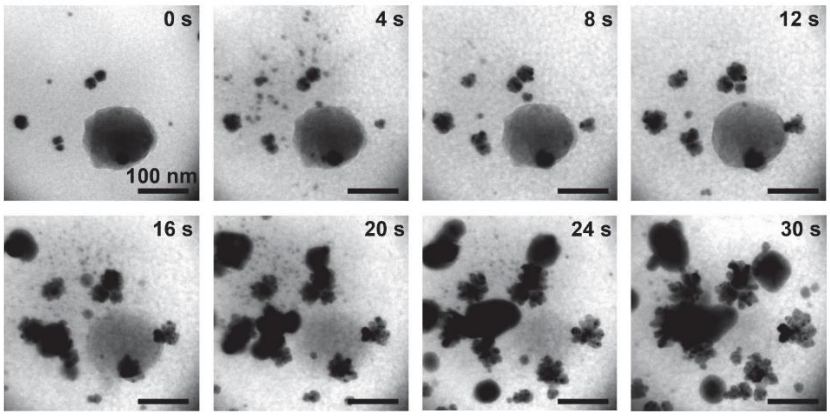

Figure 6: Electron beam-induced nanoparticle nucleation and growth. Gold nanoparticle nucleation and growth from the precursor solution from hydrated electrons.

1.4 Collagen

1.4.1 Structure and *D*-band

Collagen is the most abundant protein in the human body, distinguished by its main function of providing structural stability to tissue. Collagen is a hierarchical structure with multiple characteristic features, see Figure 7. [20]

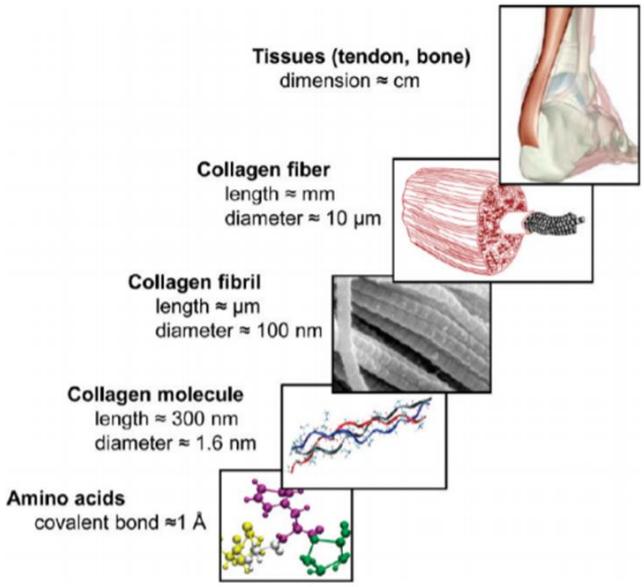

Figure 7: Hierarchical structure of collagen.[20]

The collagen molecule is comprised of a trimeric polypeptide chain with repeating amino acid triplet in the form of Gly-X-Y, where the most abundant constituents of X and Y are proline and hydroxyproline. These molecules assemble in a 5-staggered configuration, first illustrated in 2D by the Hodge-Petruska model [21], with a well-defined offset between adjacent molecules giving rise to a gap and an overlap zone. These zones are responsible for the notable *D*-band spacing of 67 nm already reported in several papers. [22–25] The *D*-band space entails an overlap and gap zone of, respectively, 40 and 27 nm. Multiples of these 5-staggered configurations further assemble in a quasi-hexagonal lattice to form the collagen fibril.

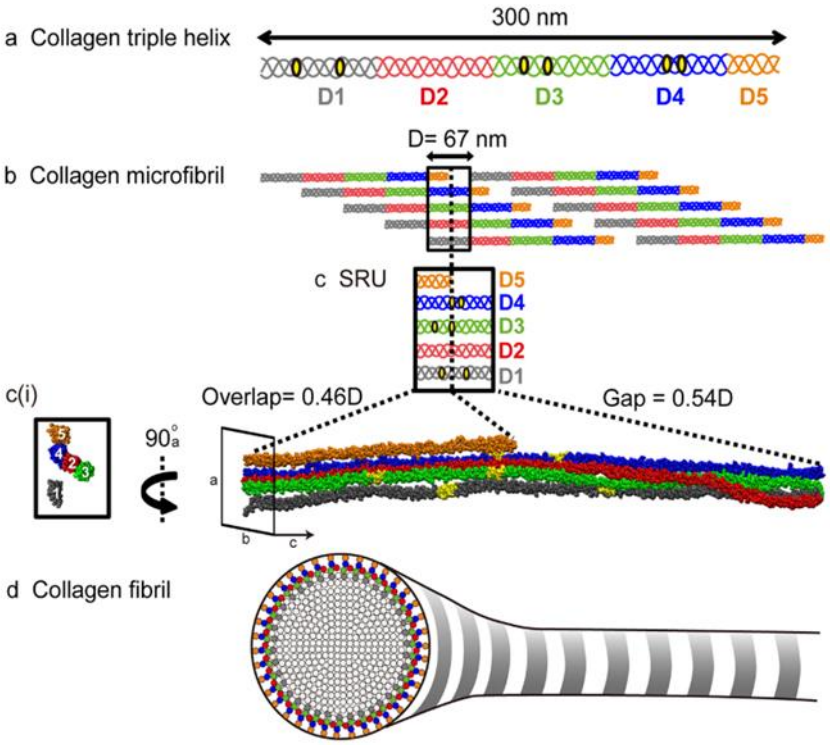

Figure 8: Formation process collagen fibril. a) triple helix building block. b) 5-staggered 2D representation with characteristic 67 nm D-band. c) 3D version of the 5-staggered configuration. d) assembly of micro-fibrils into a collagen fibril. Adopted from. [26]

Collagen fibrils can further convene to form even high order hierarchical structures, for example, tendons, bone, and skin. [27] Collagen fibrils and their hierarchical structure play an important role when it comes to mechanical behavior since it is the smallest structural unit in which the build of the hierarchical structure plays a significant role to the overall mechanical performance of the structure. Therefore, evaluation of the effect of applying tension to a collagen fibril has been extensively studied. [28,29,38,39,30–37] An important feature of such fibrils under tension is the increase in *D*-band spacing and more specifically, the increase in the gap/overlap ratio. [20] Unfortunately, the underlying deformation mechanism is still not clear, for example, whether the deformation is an homogeneous [37,40–42] or inhomogeneous process [20,32,43,44] is still on debate. Recently, studies have been performed on single fibrils either by AFM or SAXS to monitor the *D*-band spacing behavior after tension. These tools have certain disadvantages when monitoring structural changes in time on a nanoscale. In the case of AFM, the interaction of the tip with the soft matter reduces the opportunity to measure a single small area successively and the temporal and spatial resolution is not optimal. [32] The *D*-band spacing pattern obtained via SAXS is from averaging over a larger area. [41]

1.4.2 Staining

Contrast enhancement for the TEM specimen preparation remains an important pre-treatment procedure for most biological samples, since they are made up of weak scattering elements. In order to increase this lack of contrast, a benchmark method is to apply chemical staining with strongly scattering elements, for instance with heavy elements. Ideally, the heavy metal compound associates with specific features of the specimen. Two types of staining are distinguished:

- Positive staining: staining agent creates a thin film layer around the specimen.
- Negative staining: staining agent provides contrast to the environment instead of the object.

The two types of staining and the effect on collagen *D*-band spacing identification are schematically illustrated below Figure 9. [24,45,46]

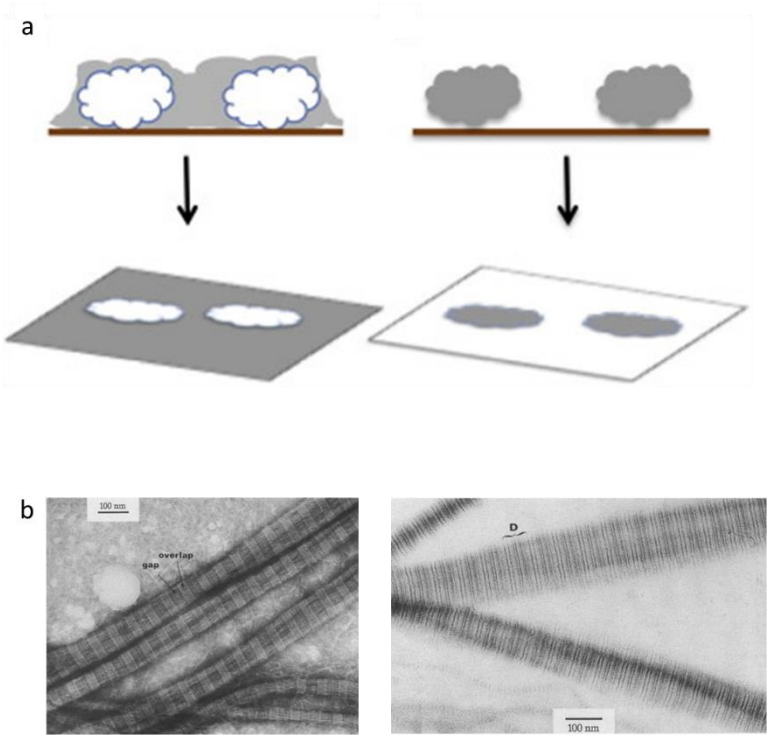

Figure 9: a) Schematic of negative (left) and positive (right) staining.[45] *b) Negative (left) and positive (right) of collagen fibrils.* [24]

1.4.3 Mineralization

Enhancing the mechanical strength of collagen is paramount for structural functions, such as bone and tooth. This enhancement is achieved in nature by mineralizing calcium phosphate (CaP) in the hierarchical porous substructures of collagen. Little is known about the effect of collagen matrix confinement and the role of non-collagenous proteins (NCPs) on the nucleation of CaP minerals. Experimental evidence demonstrates that nucleation is depending on whether it occurs extrafibrillar or intrafibrillar, see Figure 10. [47] However, the mechanisms behind the transport, infiltration, and transformation of amorphous calcium phosphate (ACP) into minerals remain unclear. [22,47–50]

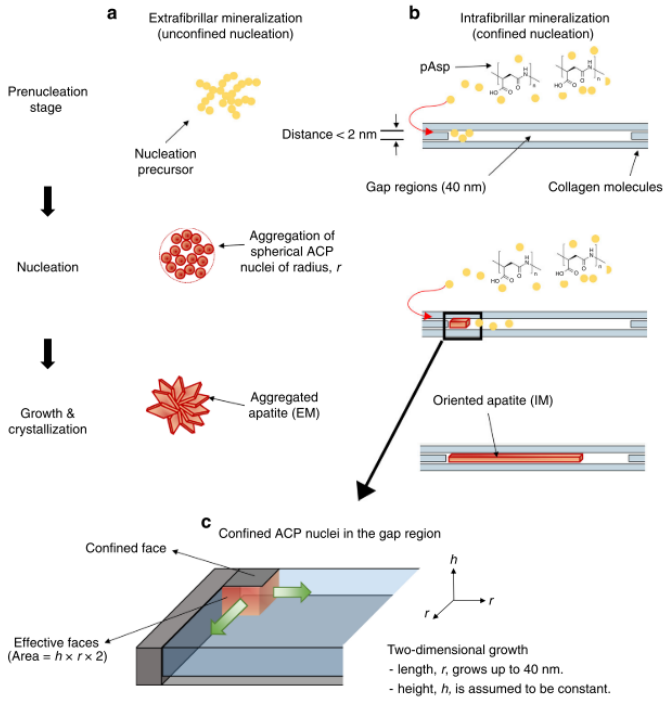

Figure 10: Different types of CaP mineralization. a) extrafibrillar nucleation, b) intrafibrillar nucleation, and c) confined space growth. [47]

1.5 Aim of this research

This thesis aims at developing *in-situ* TEM techniques to study the collagen structure and dynamics in different conditions. First, the deformation behavior of single collagen fibril is monitored under tension at real time; the high temporal and spatial resolution of the TEM allows for precise and fast monitoring of the structural changes occurring on fibril level during strain. The contribution of this work to the collagen stretching debate is reported in chapter 2.

Second, a new LP-TEM workflow is developed to probe the collagen native structure and even the mineralization process in solution. Chapter 3 will describe the method development results of this thesis towards LP-TEM of collagen mineralization. The method development comprises:

- Single collagen fibril preparation: cryo-milling.
- Sample loading and liquid cell assembly: ultra-low volume liquid handling system.
- Optimization of the TEM protocol to be able to analyze these soft matter materials without significant damage.

Chapter 2 *in-situ* Observation of collagen stretching

With *in-situ* TEM real time image series of how fibrils behave under tension are recorded. Upon analysis of these image series, it is possible to confirm the inhomogeneous mechanical behavior of collagen reported in several studies. [32,44]

2.1 Materials and methods

2.1.1 Collagen suspension

The collagen suspension is obtained using the method described in detail in 3.2.1 .

2.1.2 Chip preparation

The liquid cell consists of two chips, a bottom and top chip, each of which contains a 50 nm thick electron transparent Silicon Nitride window (DENS-solutions BV). The chips are firstly solvent washed by using acetone, ethanol, and isopropanol in the order mentioned for two minutes per solvent, and subsequently plasma treated for ten minutes at 20 Watts using oxygen as carrier on an Emitech K1050X.

The latest version of the chips on the market no longer have a protective film layer that must be washed out and, therefore, are only plasma treated for one minute at 20 W. This ensures a slightly hydrophobic surface which is ideal for precise droplet placing and assists in maintaining a hydrated sample thanks to reduced surface area of the droplet.

2.1.3 Sample loading

The collagen suspension is directly deposited on the bottom chip using an Eppendorf micro-pipette. A droplet with the size of 1 µL is placed on the bottom chip and allowed to dry. The obtained chip is placed inside the TEM holder.

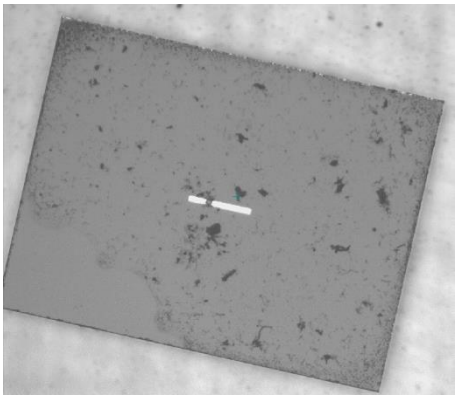

Figure 11: Collagen suspension deposited on a bottom chip using Eppendorf micro-pipette.

2.1.4 TEM analysis

TEM imaging is performed on a FEI Technai 20 (type Sphera) operated at 200 kV equipped with a LaB_6 filament and a 1k × 1k Gatan CCD camera. Movies are captured using the software package TEM Imaging & Analysis (TIA).

2.1.5 Data analysis

Images are formatted to a stack (MRC format [51]) using MATLAB and the obtained image series are analyzed using both TIA and Fiji software. For selected frames, the *D*-band spacing at three different positions along the long axis of the fibril and the length of the fibril are measured. The fibril length is determined from two fixed reference points, as shown in Figure 12.

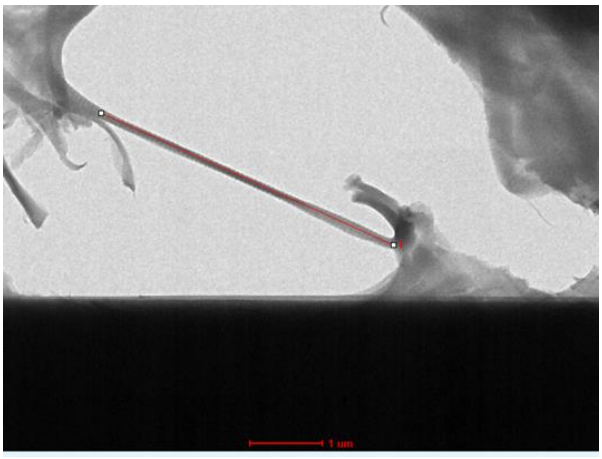

Figure 12: Length determination fibril. Reference points are at fixed points of the fibril, bottom at the bend, top at the intersection with another feature.

The *D*-band spacing is obtained by plotting a line profile of a fixed length in Fiji, which will be referred to as a segment, along the long axis of the fibril. For each segment a peak to peak distance is determined from the plot profile as shown in Figure 13b. The distance between the first and last peak is divided by the number of peaks to obtain the average *D*-band spacing. This procedure is performed three times along the length of the fibril to obtain an average *D*-band spacing. Strain mentioned in this thesis is based on the engineering strain and is calculated using Equation (2).

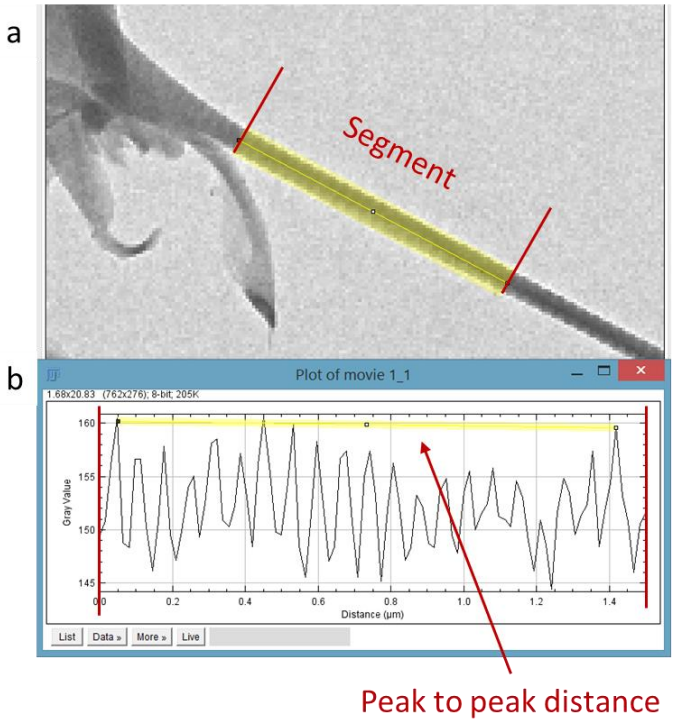

Figure 13: D-band spacing calculation. a) Positioning of the line profile on the long axis of the fibril. Line profile broadness is equal to roughly eightfold pixel distance. b) Determination of the total number of peaks and peak to peak distance from the plot profile.

$$Strain\ [\%] = \frac{Elongation}{Original\ Length} * 100\% = \frac{\Delta L}{L_0} * 100\% \qquad (2)$$

2.2 Collagen stretching

Whether collagen fibrils deform via a homogeneous or inhomogeneous route is still on debate. Being able to visualize fibril behavior under tension could lead to new insights into the collagen deformation mechanisms. Multiple collagen fibrils that are scattered across the broken window material provide the opportunity to observe fibril deformation since the electron beam causes the silicon-nitride window to deflect, indirectly applying tension to the collagen fibrils. Although the deflection is uncontrollable, it provides strain to the fibrils covering the gaps. Several image series are captured to follow this mechanical process. Figure 14 presents the overview of different fibrils, (a) the window area of the first image series and (b) the window area of the second image series measured one month later. Figure 14c shows a schematic representation of the timeline while imaging the first window area to highlight that Fibril 1 is not measured consecutively. Fibril 1 and 2 stretch with visible *D*-band spacing and provide information regarding strain effects on *D*-band spacing and overall length changes. Fibril 3 displays necking behavior under tension, however, the *D*-band spacing is too difficult to be determined due to lack of contrast.

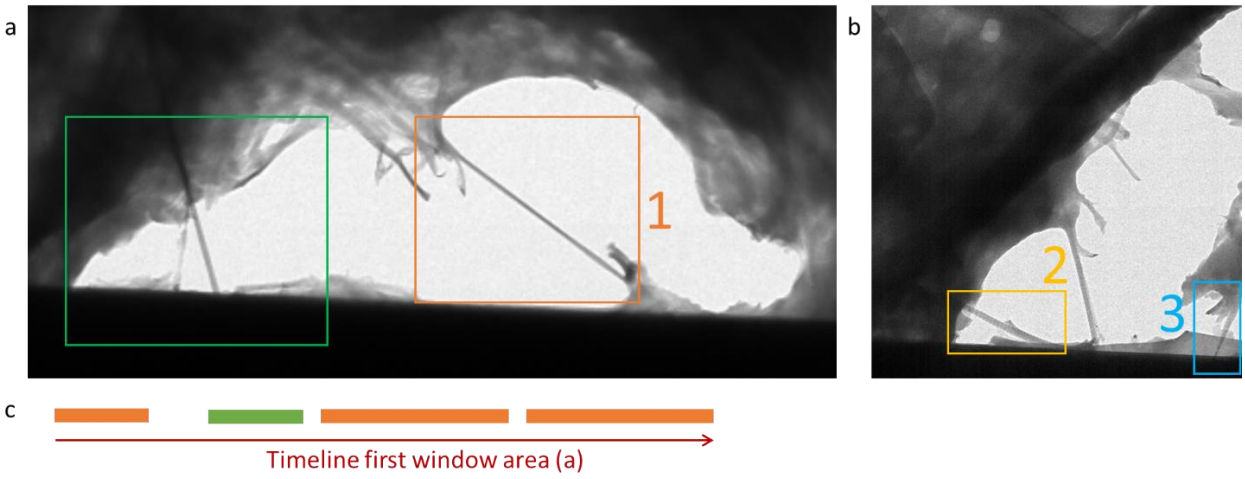

Figure 14: Overview of the different fibrils imaged. a) First window area displaying Fibril 1 and the control experiment. Imaged at dose rate 7.5 e^- nm^{-2} s^{-1}. b) Second window area displaying Fibril 2 and 3. Imaged at dose rate 5 e^- nm^{-2} s^{-1} and 21 e^- nm^{-2} s^{-1} respectively. c) Timeline at which images of the first window area are obtained.

2.2.1 Overall changes under strain

Figure 15 presents the strain and *D*-band spacing behavior of the stretched fibrils over time. Fibril 1 is stretched slowly up to almost 80 % strain and the strain vs time data are plotted in Figure 15 with orange dots. However, this deformation has not been imaged in a continuous series, resulting lack of data for this fibril in the time between approximately 350 and 1750 s. in this time window, an adjacent area was monitored (as indicated in green by the timeline in Figure 14c). In order to bridge the gap in strain data for Fibril 1, it has been observed that the window material deflected by the electron beam is the same material attached to Fibril 1, therefore, by measuring the displacement of the window material, the additional elongation (strain) of Fibril 1 is estimated. This estimation is visualized by the green set of data points in Figure 15c. The starting position of the green set is determined by plotting a fit through the orange data points. The remaining data points are calculated based on the extension of the window material added to the strain fixed for the first point. Despite not having images to confirm, the used approach provides data points that are all in line with the extension of Fibril 1. Fibril 2 is measured one month after Fibril 1 and in order to superimpose the data in Figure 15c the *D*-band spacing is used. The first *D*-band spacing measured for Fibril 2 is 76 nm and this point is placed in Figure 15d to obtain a superimposed time. The obtained time is then used to plot the straining data in Figure 15c. Both Fibril 1 and 2 experience loss of periodic *D*-band spacing. This loss of periodicity in *D*-band spacing could be attributed to internal sliding or slipping of collagen molecules when strains >30 % are achieved. [20] Further in-depth analysis regarding *D*-band spacing changes will therefore focus on the first orange data set. The strain applied to Fibril 1 is approximately 22.4 % while the *D*-band spacing increases on average by 9.1 %. *D-band* spacing is reported in literature to increase by 40 % of the applied strain; when calculating it for the here reported case results to 9.0 %, in perfect agreement with the measured value in this study. [29]

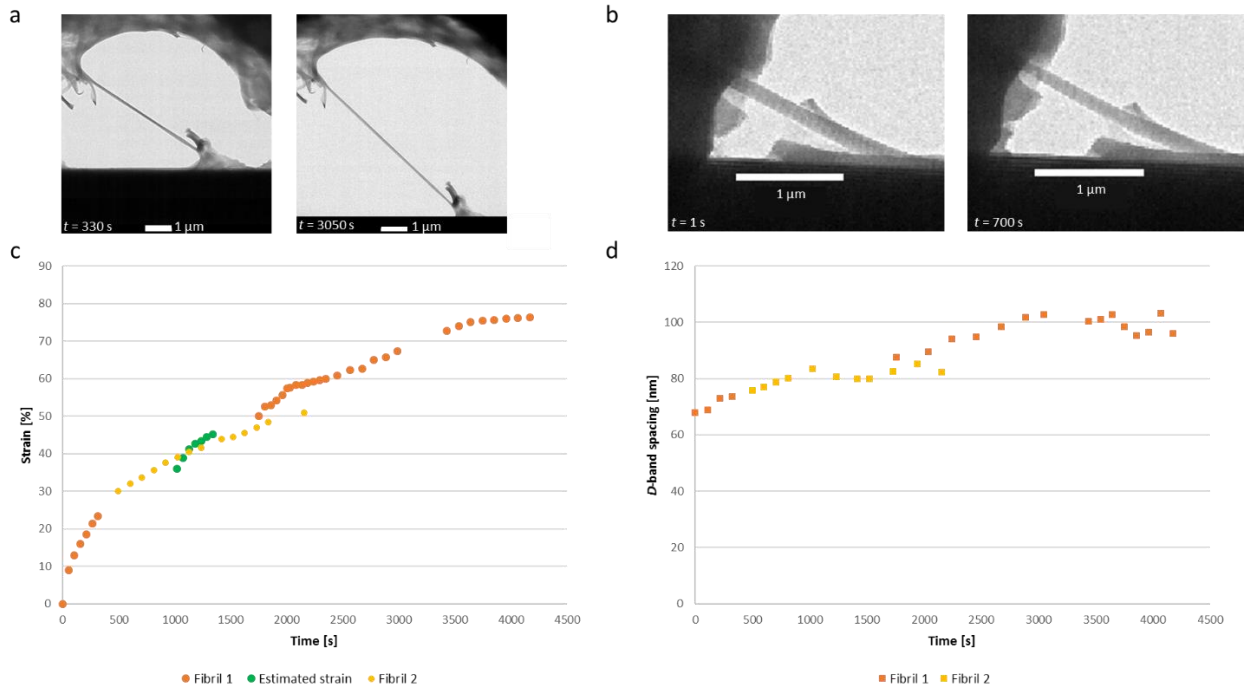

Figure 15: a) Timeframes 330 and 3050 illustrating the elongation of the Fibril 1. b) Original timeframes of Fibril 2 that are superimposed on the timescale of Fibril 1. c) Strain of Fibril 1 as a function of time with Fibril 2 superimposed, , additionally the estimated strain from the adjacent area of Fibril 1. d) D-band spacing as a function of time with Fibril 2 superimposed.

2.2.2 Local *D*-band spacing changes

To understand how the local structure changes under tension, the individual *D*-band spacing is tracked during stretching, as shown in Figure 16 and Appendix 1: Local segment change. The orange pattern, representing frame 332, extends compared to the blue pattern, frame 10, as expected based on the average increase in *D*-band spacing upon strain. It is found that the increase in each segment is not equal.

Figure 16d shows the overview of the averaged *D*-band spacing in each segment. The averaged *D*-band spacing across all segments at frame 10 and 332 are indicated by the blue and orange dashed line, respectively. Segments 4 and 5, and to a lesser extent, segments 3, all display deviating behavior from the average increase. Segments 4 and 5 indicate a smaller increase in *D*-band spacing compared to the average while segment 3 depicts a larger increase in *D*-band spacing. These results therefore prove that the increase in *D*-band spacing is not a homogeneous process and is possibly driven by small local defects that generate inhomogeneous deformation. This inhomogeneous mechanical behavior has been suggested or observed earlier. [32,44,49]

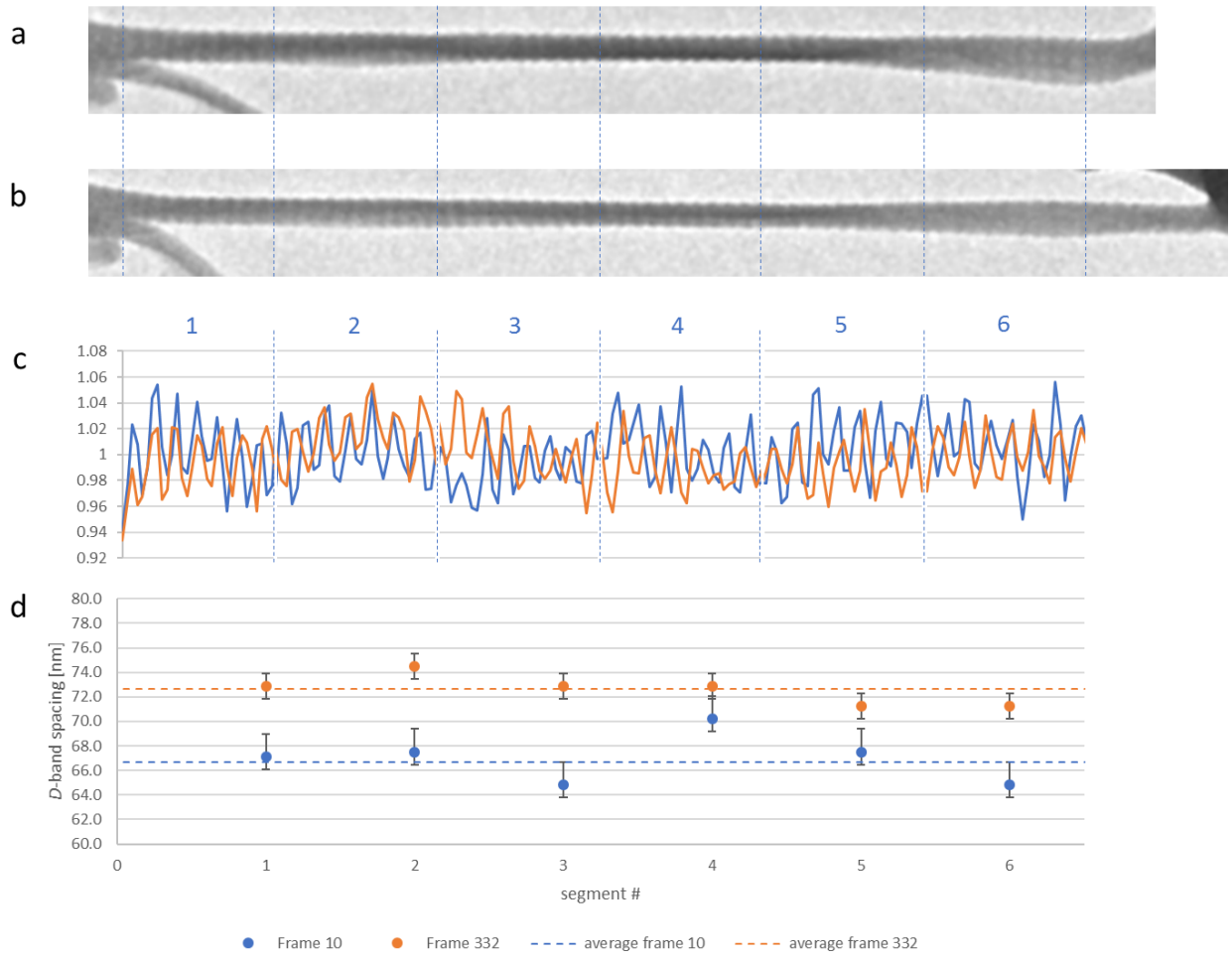

Figure 16: Fibril image of frame 10 (a) and 332 (b). c) Normalized intensity profile of frame 10 and 332 devided in six individual segments to evaluate local changes in D-band spacing. d) Dashed lines represent the average of the frame and the dots represent the individual D-band spacing of each segment. Varying increase in local D-band spacing increase.

2.2.3 Necking

The observation of necking in the stretched collagen fibril further confirms that collagen stretching is an inhomogeneous process. Fibril 3 in Figure 14b is subjected to a higher strain, greater than 100 %, and eventually breaks. When strain has reached above 30 %, the *D*-band spacing of this fibril is no longer visible. The inability to determine the *D*-band spacing is due to the loss of periodic structure.[20] Although it was not possible to follow the *D*-band spacing, the fibril breaking gives valuable insight into possible mechanisms related to the rupturing of a fibril. Both homogeneous [37,40–42] as well as inhomogeneous [20,32,43,44] behavior of collagen fibrils under tension have been reported before, but as indicated in Figure 17, inhomogeneous mechanical response plays a significant role in the deformation behavior of a collagen fibril. Figure 17 displays the diameter development of three regions just before and after the fibril breaks.

The change in diameter is only significant at the breaking point (blue circle) while the other two regions stay approximately constant (red and orange circles). In case of homogeneous distribution of the force, it is expected to see a different rate in diameter change depending on the starting diameter. However, both the 70 nm and 40 nm region display similar behavior whilst the 25 nm region experiences a significant diameter reduction. These phenomena further indicate that stress is not equally distributed within the fibril leading to so-called necking behavior where the weakest section will experience the highest deformation. Additionally, below the orange marked region there are additional signs of necking. The occurrence of necking further supports the inhomogeneity of the fibril internal structure.

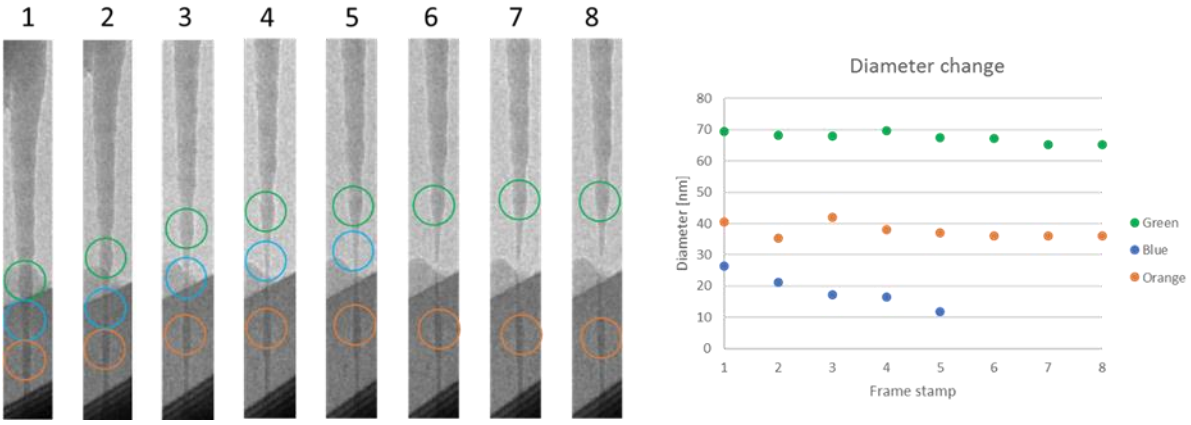

Figure 17: Diameter changes of selected regions of a collagen fibril with necking behavior illustrated at the blue circles.

2.2.4 Mechanistic discussion

Figure 18 shows schematically the changes in *D*-band spacing after stress is applied to a collagen fibril and more specifically the gap/overlap ratio.[20] It is found that locally the increase in *D*-band spacing is not homogeneous across the fibril. Assuming that the gap is most vulnerable to strain, it could lead to a local difference between the gap/overlap ratio increase in agreement with the visualized local change in *D*-band spacing increase. Therefore, it is hypothesized that upon deformation, the increase in gap/overlap ratio is inhomogeneous along the fibril and caused by small local defects in the substructure of collagen fibrils. Other evidence of inhomogeneous behavior reported in literature shows that an optimized full-atom structure of a collagen fibril obtained from 100 ns simulation indicates significant variations being present in the structure that indicate presence of local defects. [49] Silver *et al.* [52] demonstrate the effect of the level of cross-linking on mechanical response. Additionally, Puxkandl *et al.* [41] and Redaelli *et al.* [33] illustrate that at higher hierarchal levels individual collagen fibrils are linked together by matrix material, proteoglycans, which could act as load transfer elements. Furthermore, Zhu *et al.* [26] provide additional evidence that fluctuations occur at the interaction surface of collagen. It is also shown by Gutsmann *et al.* [44] that collagen fibrils are structured in-homogeneously, composed of a hard shell and soft core. Figure 19 represents a comparison between the work of Gutsmann *et al.* [44] (a) and images obtained in this thesis (b). The observed structures by Gutsmann *et al.* [44] that entail backfolding, overlapping, and other phenomena supporting the inhomogeneity can also be seen in results as obtained for this thesis.

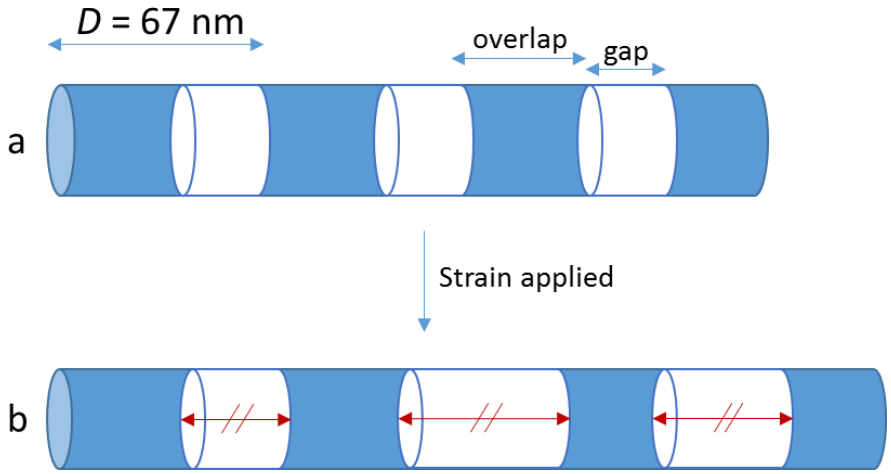

Figure 18: Schematic representation of the effect of applied strain on the D-band spacing of a collagen fibril, the increase in gap/overlap ratio has been exaggerated to emphasize the hypothesis that the ratio increase is not homogeneous. a) Fibril without strain applied with uniform D-band spacing and constant gap/overlap ratio. b) Stretched fibril with increased D-band spacing and gap/overlap ratio. Gap/overlap increase is not uniform across fibril.

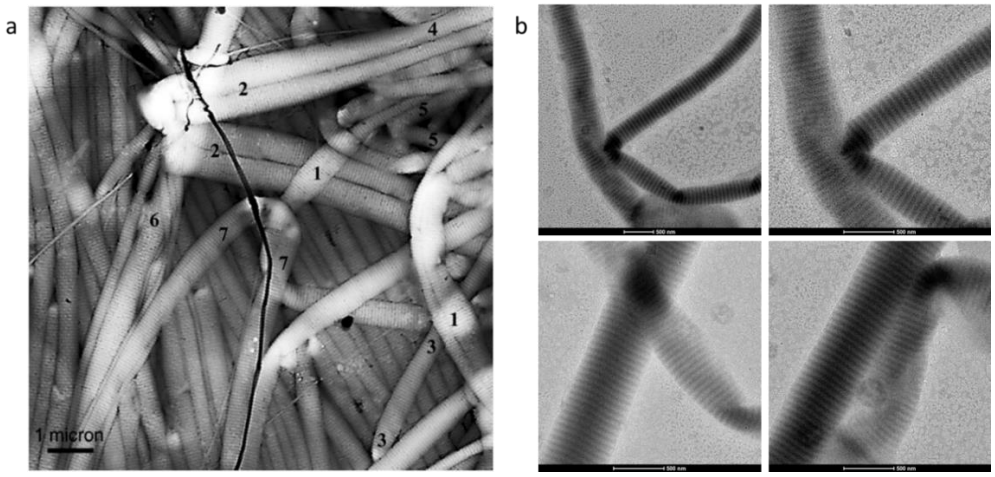

Figure 19: a) AFM images indicating specific folding and overlapping phenomena common for hand shell soft core materials.[44] b) Current in-situ TEM work illustrating similar effects of folding and overlapping.

2.2.5 Electron beam effects

To confirm that the *D*-band spacing behavior is not affected by the electron beam during stretching, a threefold electron flux is used, in comparison to initial stretching experiments, to image a collagen fibril that is not subjected to a mechanical force. Figure 20 illustrates the *D*-band spacing over approximately 450 s of a fibril attached on one side of the damaged window. *D*-band spacing does not change during imaging, meaning the electron beam effects are negligible. Based on this observation, it can be concluded that continuous irradiation of the fibril is not leading to changes in the *D*-band spacing.

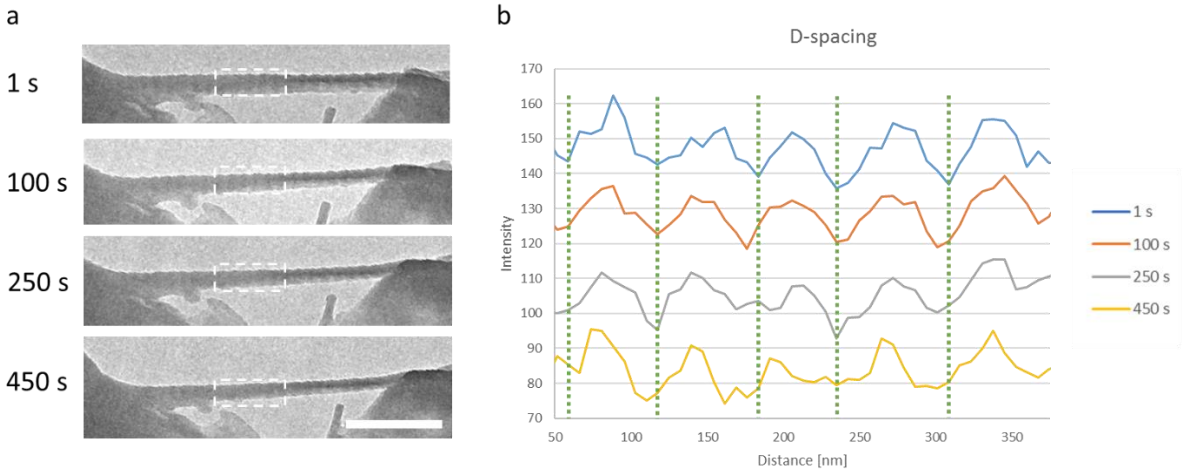

Figure 20: Electron beam investigation on single collagen fibril at 21 e^{-} nm^{-2} s^{-1}. a) TEM images of the single collagen fibril in time. Scale bar: 500 nm. b) Corresponding D-band spacing intensity profiles from dashed box in (a).

2.3 Conclusions

In summary, *in-situ* TEM reveals the inhomogeneous mechanical behavior of collagen. It is demonstrated that biological materials can be visualized for long periods of time using the low dose strategy. *D*-band spacing displays a distribution of lengths with an average close to 67 nm. Collagen fibrils in vacuum can withstand strain up to 80% without failure. Upon strain the *D*-band spacing and in particular the gap/overlap ratio increases as expected, however, it is shown here that this increase is not homogeneously distributed along the long axis of the fibril. Presumably connected to the local differences in strain, necking occurs at large deformation eventually leading to breaking of the fibril.

Chapter 3 LP-TEM of collagen

A common challenge in biological research is visualizing the dynamics that are responsible for biological functions. Addressing this challenge involves the development of innovative microscopy techniques to study these dynamics at nanoscale. [7] The development of LP-TEM allows for the application of the strong capabilities of electron microscopy to analyze liquid samples. Traditionally the examination of liquid based processes was only possible by freezing or drying of the sample. With the development of LP-TEM it is now possible to examine the structure and dynamics of biological materials at high temporal and spatial resolution. The use of LP-TEM technology has aided, amongst others, recent developments in the fields of electrochemistry, phase transformation in liquids, and life sciences. [5] The ability to analyze in real time the formation of crystalline mineral phases is of high interest in the field of collagen mineralization. Collagen structures and mineralization processes have been extensively studies by cryo-TEM, AFM, and *in-situ* SAXS and wide angle x-ray diffraction (WAXD), leading to several new insights regarding the ACP transport, *D*-band spacing, and intrafibrillar mineralization. [47,48,53] However, high temporal and spatial resolution on the dynamics behind mineral collagen interaction and the formation for CaP crystals in a liquid environment is lacking. Applying LP-TEM to investigate the collagen structure and mineralization process might solve remaining questions. Typical challenges in imaging soft matter in liquid is the inherent low contrast and high beam sensitivity, therefore, sample preparation methods and imaging protocols must be developed.

This chapter mainly focusses on developing new LP-TEM preparation procedures towards visualizing the collagen structure and its mineralization in aqueous environment. Contrast optimization is achieved by staining and controlling thickness. Thickness is controlled by introducing an ultra-low volume liquid handling system. To the author's knowledge, this is the first-time collagen is imaged in aqueous environment using LP-TEM. Furthermore, efforts towards applying the information obtained from bulk mineralization into guiding the experimental design of the confined space of the LP-TEM are reported.

3.1 Materials and method

3.1.1 Collagen suspension

The collagen suspension is described in section 3.2.1 .

3.1.2 Collagen mineralization

To study the CaP mineralization [54,55] the following chemicals were used: HEPES buffer (Sigma), $CaCl_2$ (VWR), K_2HPO_4 (Merck), and poly-DL-aspartic acid (pAsp) 2-11 kDa (Sigma). Stock solutions were prepared in milli-Q water and stored in the fridge at 6 °C. To assist dissolution both HEPES and $CaCl_2$ were sonicated for two minutes. pAsp solution is kept for maximum a week since it is prone to bacterial contamination. Note: milli-Q water has a pH of approximately 5.4.

3.1.3 Collagen staining

Staining was performed using Phosphotungstic acid (PTA, Sigma) dissolved in milli-Q water with a mass fraction of 2 % as staining agent. [21,24,45,46]

3.1.4 sciTEM

The sciTEM (SCIENION AG, Berlin, Germany) is an ultra-low volume liquid handling system designed for depositing liquid sample droplets for instance on TEM liquid cell chips. [56–58] The machine consists of a high precision drive system that enables the placement of distinct sample droplets. The sample droplets are placed by a non-contact piezo dispensing technology that is capable of dosing liquid volumes as low as 100 pL. Furthermore, the non-contact loading allows droplets to be deposited onto fragile surfaces without damage.

3.1.5 TEM

TEM images were obtained with a FEI Technai (Type Sphera) microscope operated at 200 kV with a LaB_6 gun and a Ceta camera. Image analysis was performed in MATLAB and Fiji.

3.2 Tackling the challenges in LP-TEM of collagen

Beam effects and image resolution are two main limitations in LP-TEM. [5] Image resolution is mostly affected by the liquid layer, window and material thickness, and sample beam sensitivity. Beam effects originate from the applied electron dose, electron-liquid and electron-sample interactions. Imaging soft matter, such as collagen by LP-TEM, would have an increased difficulty due to the extremely high beam sensitivity and low contrast in aqueous environment, which dramatically reduce the achievable resolution. As bonding energies of such materials are close to thermal energies, collagen structure and dynamics can be easily affected by weak disturbance in the environment. So far this collagen structure and its mineralization have not been investigated with LP-TEM. In this section, the first attempt into LP-TEM of collagen is discussed in terms of challenges confronted.

3.2.1 Contrast optimization in LP-TEM of collagen

Enhancement of both, resolution and contrast, can be achieved through obtaining an ultra-thin liquid layer thickness that will ensure minimization of the inherent scattering of electrons by electron-liquid interactions. The scattering of electrons in the liquid layers is predominantly responsible for statistical fluctuations, i.e. the noise, of the signal. [7] Therefore, controlling the liquid layer thickness will assist in obtaining a signal to noise ratio (SNR) that is high enough to diminish these statistical fluctuations. More precisely, based on Rose criterion, only when the SNR exceeds a value of 3 to 5, the object can be detected. In this section developments into controlling the liquid layer thickness in LP-TEM are discussed. Additionally, staining as a typical contrast enhancement technique has also been tried and reported here. Please note that achieving a thin liquid layer thickness through adaptation of the liquid cell configuration or material is not discussed here.

3.2.1.1 Liquid layer thickness control

Sample thickness control. Ensuring that a collagen sample is thin enough for LP-TEM requires the use of single collagen fibrils rather than large aggregations. Single collagen fibrils can be obtained from bottom-up or top-down method. The method for bottom-up assembly of amino acids into collagen fibrils is being researched extensively both in this group and in other institutes. However, this method has not been well established yet and it is also difficult to extract single fibrils from resulting bottom-up assemblies. Therefore, a top down approach is employed where a piece of collagen tape will be used as starting point. Ideally a dispersion of individual fibrils is obtained to ensure consistent thickness and high sample reproducibility. The following cryo-milling strategy has been developed: (1) A 2 cm sample of resorbable collagen tape (ACE, reference number 5091000) is placed on sterile paper and hydrated using a few droplets of milli-Q water; (2) the hydrated sample is gently placed in a mortar and frozen using liquid nitrogen; (3) the sample is grinded, while periodically adding liquid nitrogen, until a fine powder is obtained in which no friction can be felt; (4) the powder is freeze dried overnight to remove all water and then used for preparing a collagen suspension (5). A 1 g/L to 5 g/L suspension is made using milli-Q water and sonicated for 60 min. Larger fragments present in the suspension are allowed to settle and a sample of the supernatant is used for analysis to prevent damage to the liquid cell windows.

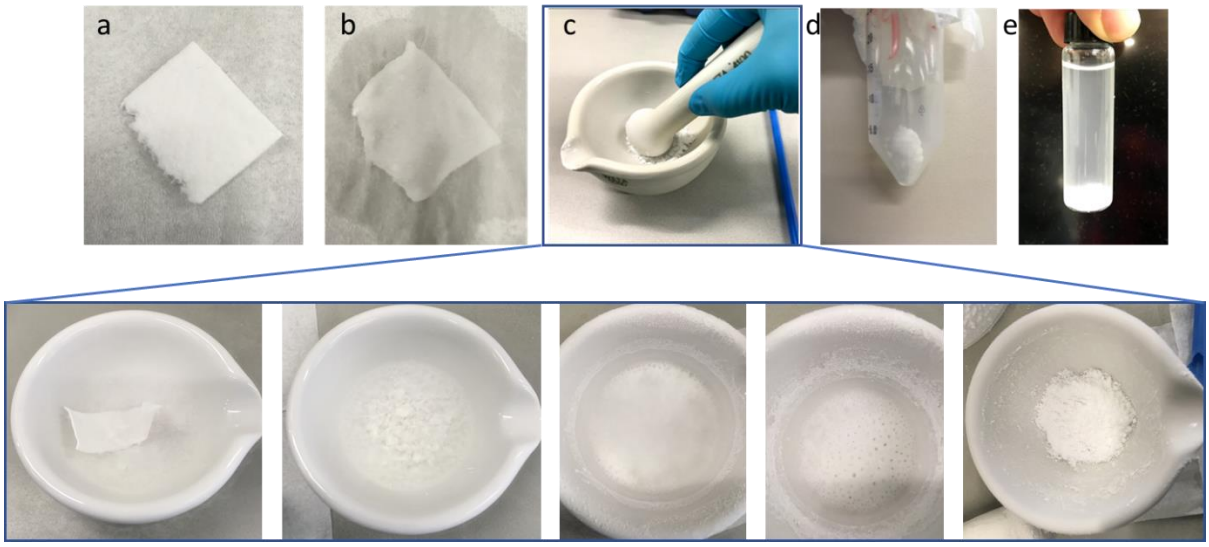

Figure 21: Collagen sample preparation steps. a) A 2 cm piece of collagen tape on sterile paper. b) Collagen tape hydrated with milli-Q water. c) Freezing and grinding of the tape using liquid nitrogen, in the dropdown structural changes from frozen tape to coarse particles to fine powder. d) Sample after freeze-drying overnight to be stored in fridge. e) Collagen suspension in which the large particles settle on the bottom and the supernatant can be obtained for further analysis.

The use of sciTEM to achieve low-volume liquid loading. Solvent thickness, or in this case water layer thickness, is a main challenge related to liquid cell thickness. Small volume liquid handling is intrinsically difficult to perform reproducibly by hand and the droplet size obtained while using a micropipette is rather large compared to the cell window, as visualized by Figure 11 where a single drop covers the entire cell surface. The sciTEM tool is unique and offers the possibility to deposit reproducibly at specific positions well defined picolitre droplets creating consistent and thin liquid cells which are desired to minimize noise from the liquid. Furthermore, the tool has an integrated pick-and-place tool to assist in carefully assembling the liquid cell and ensuring precise chip alignment achievable through automated recognition. Applying the sciTEM tool minimizes human error by automating manual handling steps. Several different types of dispensing needles with ranging surface coatings are available, and it is found that the type 3 PDC 60 appears to be the most suited for the collagen suspension in the range of 1 g/L to 2 g/L. Increasing the concentration leads to viscosity problems upon dosing, causing fouling and loss of precise casting position. Therefore, depending on experimental requirements, different running procedures are designed in the sciTEM operating software: (1) dry mode: to precisely load a sample and let it dry for further analysis; (2) wet mode: to load a sample with distinct volume and keep it hydrated. See Appendix 3: sciTEM workflow.

Dry mode is the first step in order to reach the wet mode where the combination of position and volume play a crucial role for solvent thickness obtained in the liquid cell. As illustrated in Figure 11, the window area of the chip is limited and precise control is critical, otherwise a thick cell is obtained due to accumulation of sample. In sciTEM, sample loading spots can be predefined, and a certain number of drops can be delivered to the targeted location with tens of micrometer accuracy. As shown in Figure 22 this approach generates a well dispersed sample on the chip window.

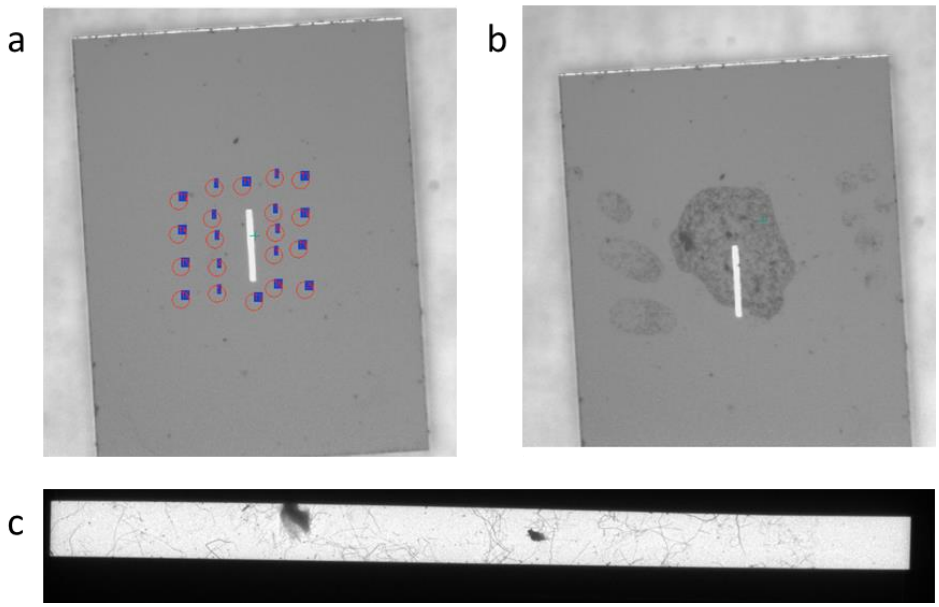

Figure 22: a) Selection of deposition positions on the chip. b) Result of the deposition, collagen around the window area. c) TEM image of the window displaying the well dispersed collagen fibrils.

In wet mode, sciTEM enables the creation of a hydrated cell which is crucial for many biological systems in addition of having precise volume deposition to control the liquid thickness. Furthermore, the sciTEM provides full process automation. An environmental chamber is used to create a saturated atmosphere around the chip to prevent water evaporating from the sample. As shown in Figure 23, the tip of the TEM holder slides into the environmental chamber from the front, and there is an opening on the top to allow sample deposition and cell closure. A slot outside the chamber is designed to maintain the top chip for automated closure after sample deposition. Inside the chamber a layer of water together with a folded piece of wetted paper is used to generate the saturated atmosphere. The LPEM protocol retrieves the suspension from the micro-titer plate and deposits it on the chip. After the top chip is placed onto the bottom chip, an image is taken to verify the cell assembly. It is important to keep in mind that the time between sample deposition and closing by placing the top chip is approximately 25 s. Tests have revealed that the water layer will start to evaporate despite the environmental chamber as visualized below, however, this process takes roughly 7 minutes which is significantly longer the closing procedure.

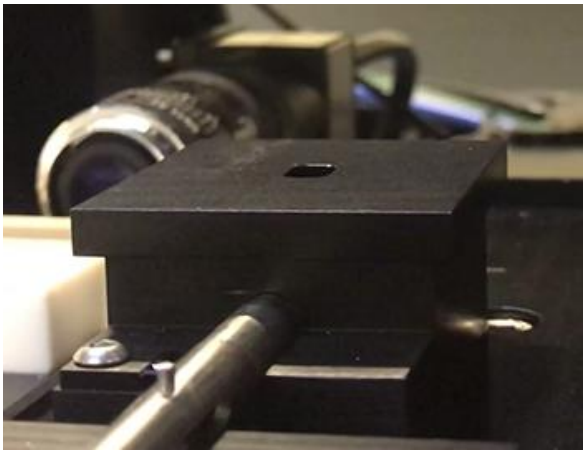

Figure 23: Environmental chamber for the sciTEM system to ensure saturated atmosphere.

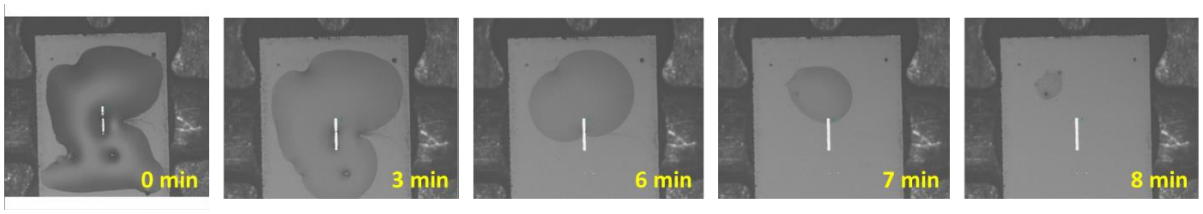

Figure 24: Evaporation of the water inside the environmental chamber of the sciTEM.

With the assistance of sciTEM, it is feasible to deposit a well-defined liquid volume into the liquid cell with picolitre accuracy. As demonstrated in Figure 25, three different liquid volumes (27 nL, 54 nL, and 78 nL) are patterned by sciTEM with predefined array. Each drop is approximately 300 pL. TEM confirmed that both the 27 and 54 nL samples are dry. The 78 nL experiment is still in hydrated state, however, the liquid layer is slightly too thick, and no collagen is visible. Despite not being able to see the collagen, another interesting phenomenon is seen, namely inward bulging of the window material due to Laplace forces as shown in Figure 26. Because the discussion is still ongoing what the origin of the phenomenon is, no further explanation is given here.

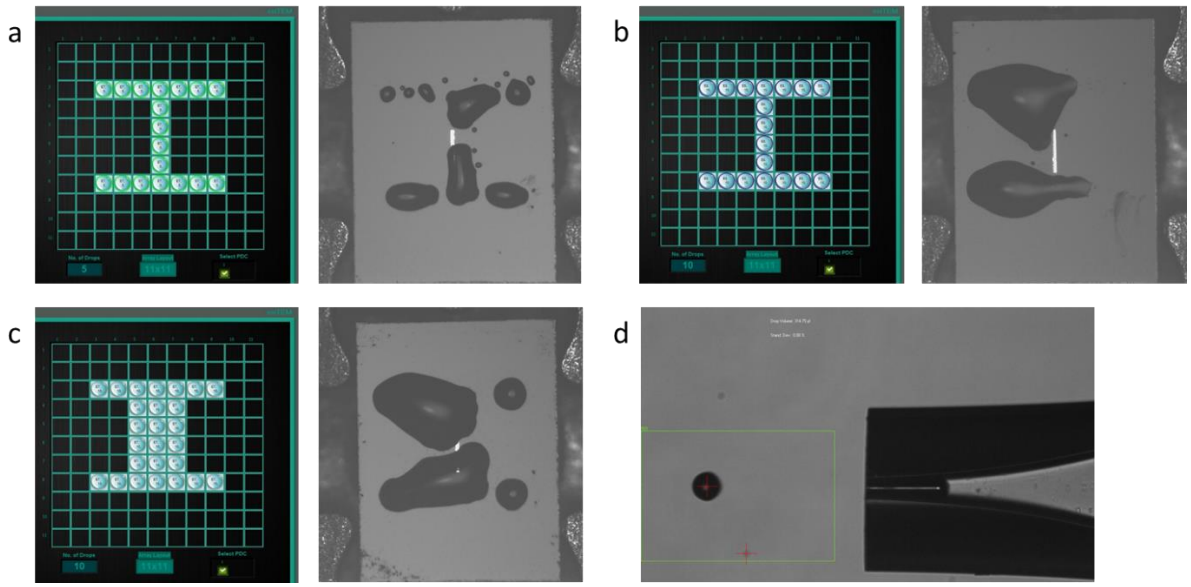

Figure 25: Varying liquid amount. a) 27 nL, b) 54 nL, c) 78 nL. d) Droplet volume detection.

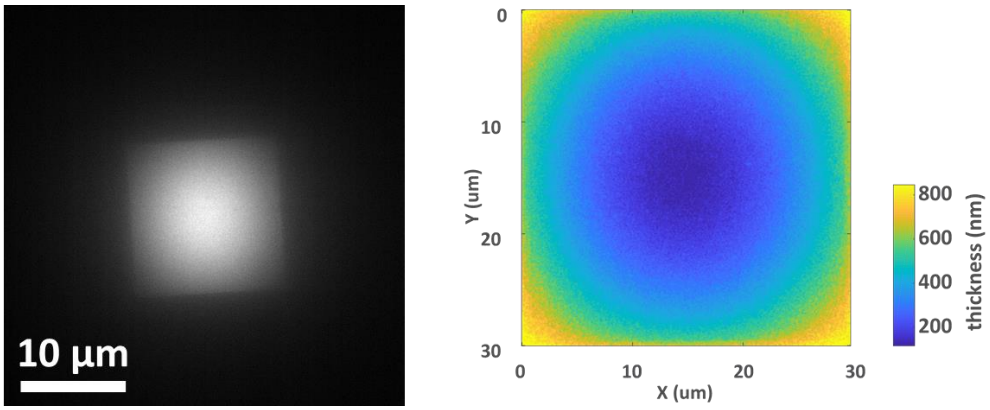

Figure 26: Left TEM image of the hydrated liquid cell and right the liquid thickness mapping from the intensities indicating inward bulging.

To predefine the liquid thickness in the liquid cell, chips with a 200 nm spacer were used. Here the new type of chip is tested, and initial testing indicate that these chips are not ideal for the collagen suspension, as they seem to be more suited for addition of a homogeneous solution. Upon adding a suspension to the chip, particles end up on the spacer surface making it difficult to close the cell and resulting in uneven thickness across the window. In summary, these chips are not beneficial for the collagen suspension.

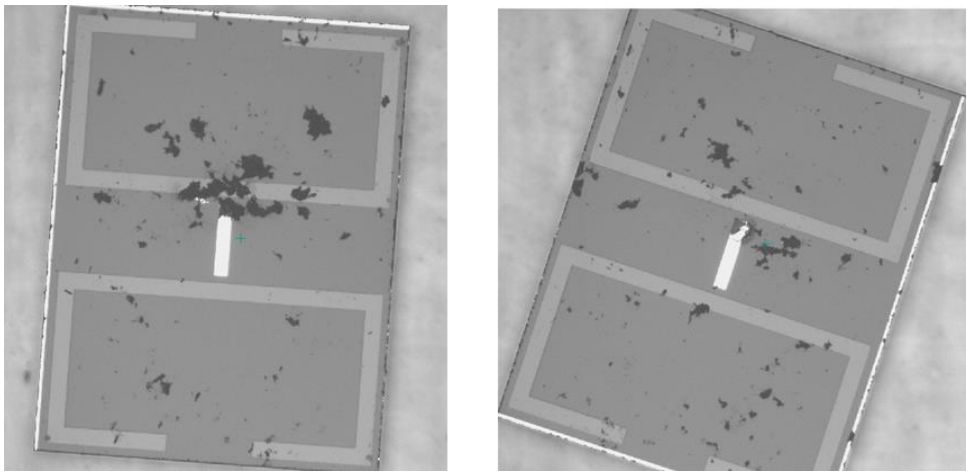

Figure 27: Collagen particles scattered across the spacer chip.

3.2.1.2 Staining

A commonly used route to increase contrast in biological samples is adding heavy metal staining agents, which is normally called staining. These compounds either form a thin layer around structural elements or bind to specific regions of a material. [24,45] The heavy metal part of these staining agents results in increased contrast due to their large scattering potential. Staining normally involves a drying and washing step to remove excess staining agent that interferes with the imaging. The initial idea in line with the optimized collagen sample preparation workflow is to stain the collagen tape before the cryo-milling. To achieve this the tape is submerged in a PTA solution with a mass fraction of 2 % (Figure 28). The submerged tape is stored overnight and afterwards treated identical to the cryo-milling steps described in 3.2.1 .

Figure 28: Collagen tape submerged in PTA solution with a mass fraction of 2 %.

The collagen obtained from section 3.2.2. is re-dispersed in milli-Q water to obtain a 2 g/L collagen suspension and deposited using the sciTEM tool on a liquid cell bottom chip for analysis. The staining agent did either not bind sufficiently to the collagen tape or substantially washed away when the sample is re-dispersed since the contrast increase is limited, as shown in Figure 29.

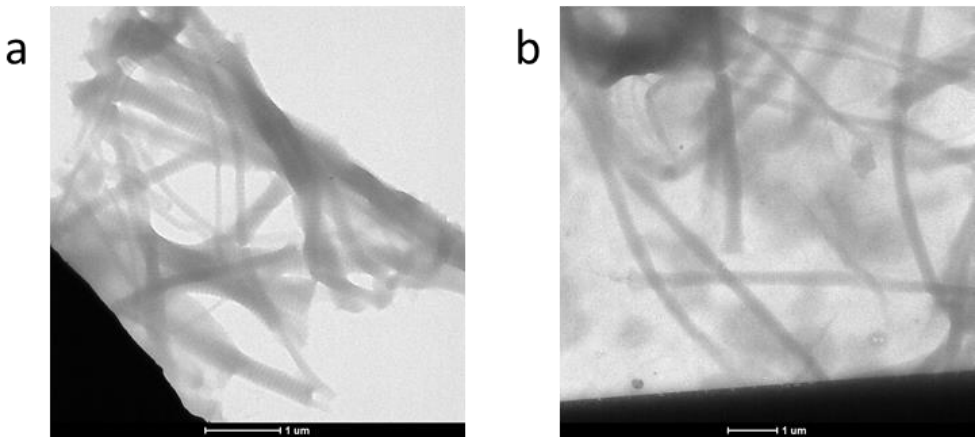

Figure 29: a) Overnight stained collagen tape. b) Unstained collagen sample.

As structural contrast is not enhanced strongly, two more experiments were performed. For the first experiment a droplet of the previously described suspension is added to a TEM grid and after drying an additional droplet of PTA solution with a mass fraction of 2 % is added and allowed to dry, this approach will be close in line with negative staining. Second, the stained collagen is re-dispersed in a PTA solution with a mass fraction of 2 % for 30 min, and thereafter a droplet is added to a TEM grid. Although, the contrast is enhanced for experiment one, it involves a fully dry sample. Achieving a negative stain in a liquid state seems very challenging. In the second experiment the increased contact time with the additional increased surface area of the cryo-milled collagen results in a more positive stain behavior where the staining molecules are attached or have reacted with the internal structure of the collagen. This increases the contrast in the liquid state; however, it is not clear whether the presence of these molecules influence the mineralization behavior of collagen.

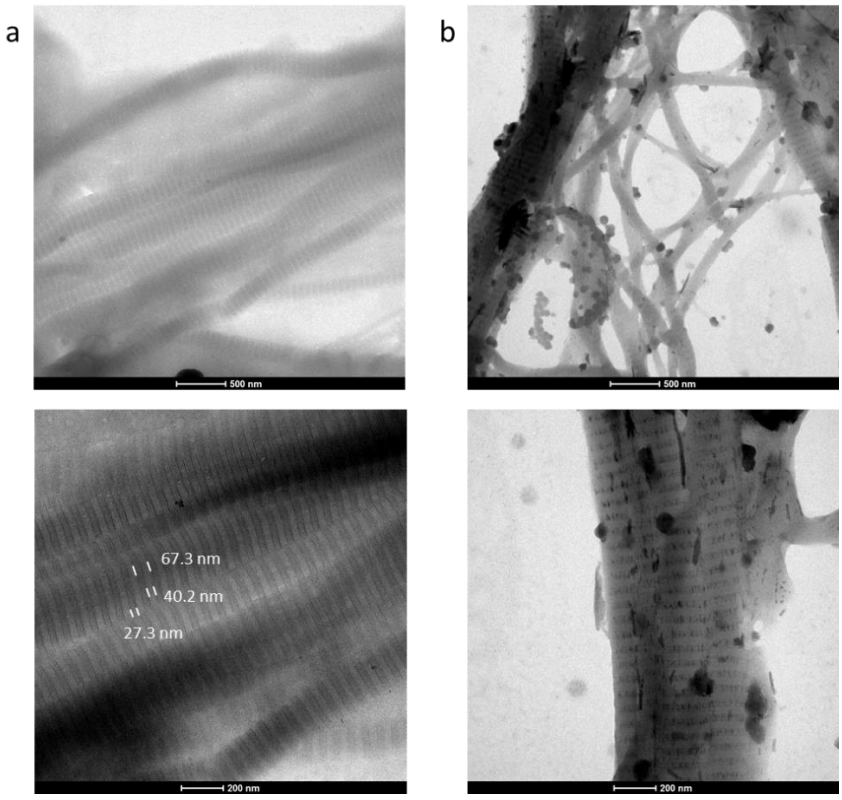

Figure 30: a) Experiment 1, additional droplet of PTA solution with a mass fraction of 2 % added to collagen suspension. Clear D-band spacing of 67 nm with corresponding overlap and gap zone of 40 and 27 nm respectively. b) Experiment 2, stained collagen re-dispersed in PTA solution with a mass fraction of 2 % for 30 min.

3.2.2 Beam sensitivity

Determining beam effects on a biological structure is not straightforward as it requires significant contrast to visualize the consequences of the electron beam. To investigate beam effects on collagens, a liquid cell that contains a large collagen agglomeration in liquid was firstly dried in air and post-mortem analysis was performed on the bottom chip as shown in Figure 31. The agglomeration appears to be still hydrated but more clearly visible. The structure is monitored over time to assess the electron beam effect. After approximately 3 min there is a significant change visible in the structure, and it remains unclear if it is caused by electron beam effects or it is due to further de-hydration of the sample. Research is ongoing to reduce beam damage effects. [59]

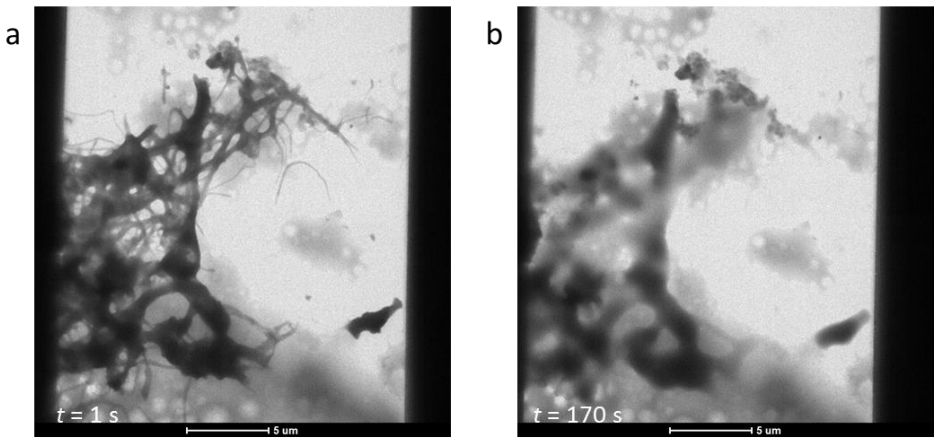

Figure 31: Visualizing possible electron beam effects, structural changes over 170 s at dose rate 1 e^- nm^{-2} s^{-1}.

3.3 LP-TEM of collagen structures

The final goal of imaging collagen in liquid as described above is very challenging and, despite many attempts, only a single experiment yielded a partial visualization of collagen in water, as shown in Figure 32. This is considered however a breakthrough in LP-TEM imaging since, to the author's knowledge, it is reported for the first time. As expected, and in line with parallel ongoing research the contrast is limited. In low magnification, the high scatter indicates that the total thickness is not optimal. Figure 32b and c (blue box) show the changes that occur in time, either due to beam damage or movement of the collagen, which make the analysis of this structure very challenging. Figure 33 shows the line profile of a selected area with a SNR of 3.8, calculated using (3), and it illustrates, in agreement with the Rose criterion, the difficulty in identifying a structure and especially the small structural features of collagen.

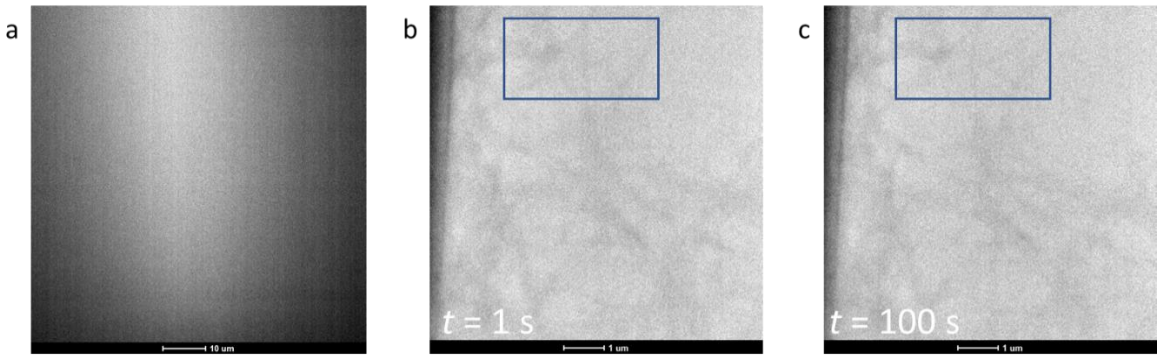

Figure 32: liquid phase TEM of collagen. a) low magnification image indicative for sub-optimal thickness. b) higher magnification image with collagen structure present in water at initial time. c) same position image in a later time with clear structural movement (blue box).

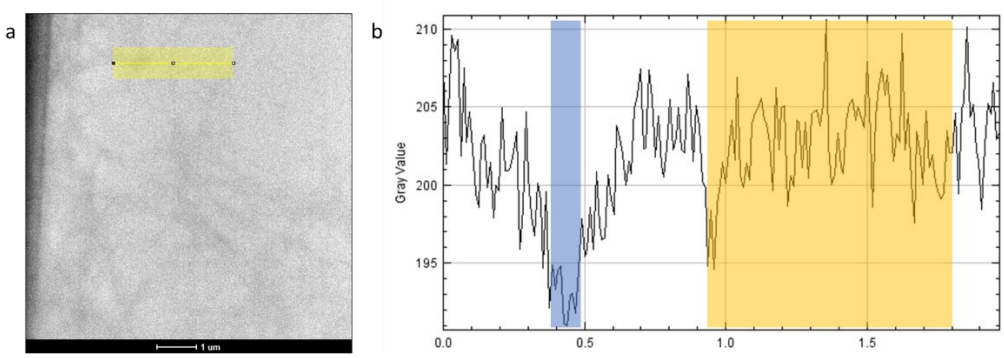

Figure 33: Determination of the SNR of a collagen fibril in a LP-TEM image. a) The LP-TEM image with the line profile of area of interest. b) Line profile data divided in structure signal (blue) and background signal (yellow).

$$SNR = \frac{\left|Average_{signal} - Average_{background}\right|}{\sigma_{background}} \quad (3)$$

3.4 Towards *in-situ* monitoring of collagen mineralization

Being able to prepare a hydrated sample in a liquid cell will enable the opportunity to trace dynamics of a system over time. This will grant unique insight into many synthetic and biological systems and processes. Although many interesting processes have been successfully monitored [11,13,14,19], the total time of *in-situ* experiments rarely surpasses more than an hour. This leads to limitations of applying LP-TEM from some long duration reactions and processes, such as steel corrosion and mineralization process. Slow processes require sacrificing some of the temporal resolution of the TEM in order to maintain the advantage of single event tracking. Two strategies are possible to mediate this problem: (1) taking snapshots rather than continuous imaging. This approach is similar to a typical cryo-TEM protocol but with particle tracking ability and will generate significant information regarding the long-term effects, but it will sacrifice the temporal resolution; (2) performing *ex-situ* lab experiments that assist in guiding the *in-situ* experimental design. The ex-situ experiments will enable the identification of critical time ranges in which then the *in-situ* technique can be performed. In this section, in order to monitor a multiple-day-long collagen mineralization process, the second described approach is adopted and mineralization experiments in bulk solution are firstly carried out to identify interesting time segments and optimize concentrations for utilization in the liquid cell.

3.4.1 Collagen mineralization in bulk solution

Collagen mineralization in bulk solution will assist in determining ideal time segments for transfer and visualization in LP-TEM. Table 1 describes the main parameters and differences between three mineralization experiments carried out in this work. Experiments 1 and 2 are specifically designed towards introducing the mineralization process into confined liquid cell space, while Experiment 3 is the control one normally applied in lab environment. Furthermore, the concentration of collagen is optimized to be 2 g/L for sciTEM deposition in order to prevent the clogging of the nozzle. Figure 34 exhibits the mineralization results from the three different experimental conditions, as reported in Table 1. The control experiment (c) indeed shows the formation of plate-like structures inside the fibril, including swelling of the fibril. The corresponding electron diffraction (ED) pattern (f) indicates feint presence of crystalline structures. The other two experiments show infiltration of material into the fibril, however, there is no clear presence of crystal structures based on the corresponding diffraction patterns. To confirm that the crystal structures formed using the conditions of experiment 3 are indeed CaP, a control experiment with reduced pAsp concentration is performed. PAsp is known indeed for inhibiting crystal formation,

therefore, by reducing its concentration, clear crystal formation outside collagen fibrils is expected. The results shown in Figure 35 confirm our hypothesis and show structures similar to those inside the fibril of experiment 3, yet with a more defined diffraction pattern. Additionally, it is well in line with hydroxyapatite crystals grown in the absence of pAsp. [55] Optimizing the experimental parameters to obtain a bulk-solution protocol that can be used as guide for LP-TEM experiments requires further advancement in reducing the collagen concentration and changing the heating method.

Table 1: Overview of parameters used in bulk-solution collagen mineralization experiments.

	Experiment 1	**Experiment 2**	**Experiment 3**
pAsp	75 mg/L	75 mg/L	75 mg/L
$CaCl_2$	4.5 mM	4.5 mM	4.5 mM
K_2HPO_4	10 mM	2.1 mM	2.1 mM
HEPES	10 mM	10 mM	10 mM
Collagen	2 g/L	2 g/L	5 g/L
Heating method	Water bath	Water bath and Oven	Oven and Oil bath
pH tuned	No	Yes	Yes

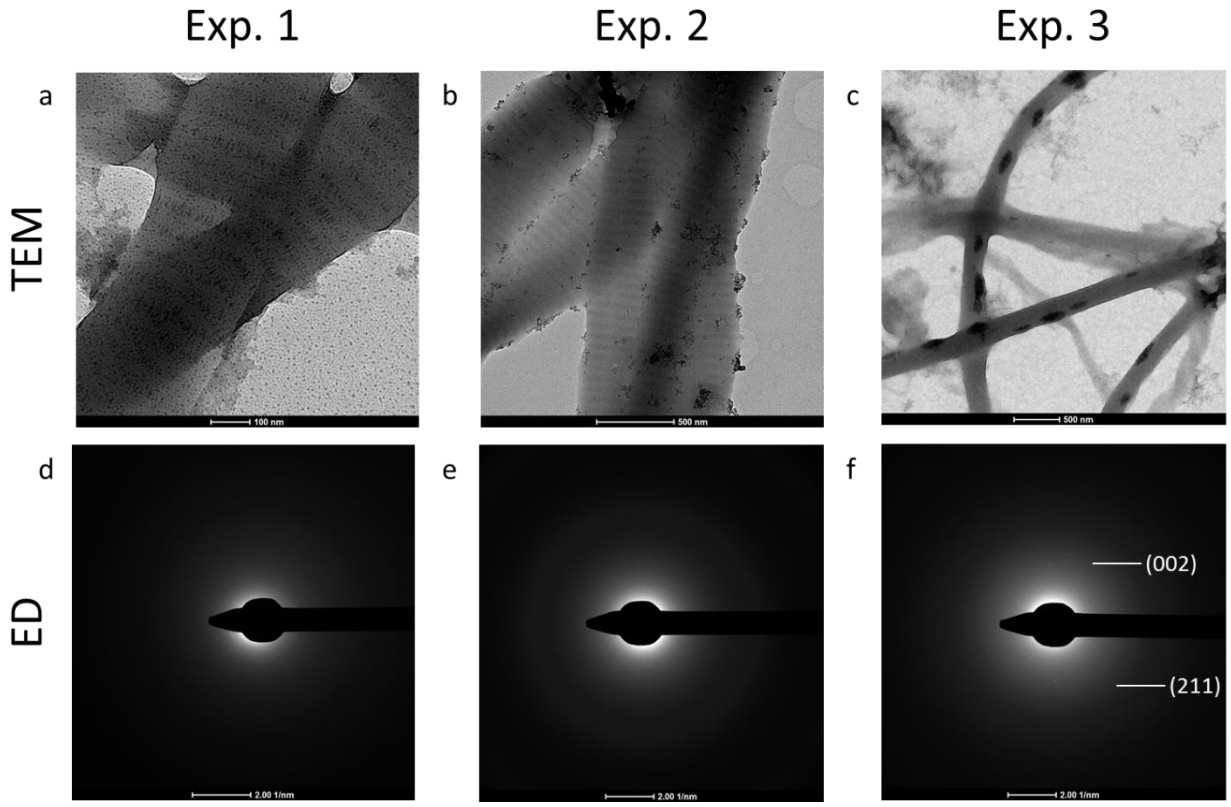

Figure 34: Lab mineralization results. a) TEM, d) ED of experiment 1, no crystalline structures present. b) TEM, e) ED of experiment 2, more structures are formed still outside fibril. No crystalline structures present. c) TEM, f) ED of experiment 3, the standardized protocol results in plate-like formation inside the fibril. Diffraction pattern indicates the presence of crystalline phase, which probably is CaP.

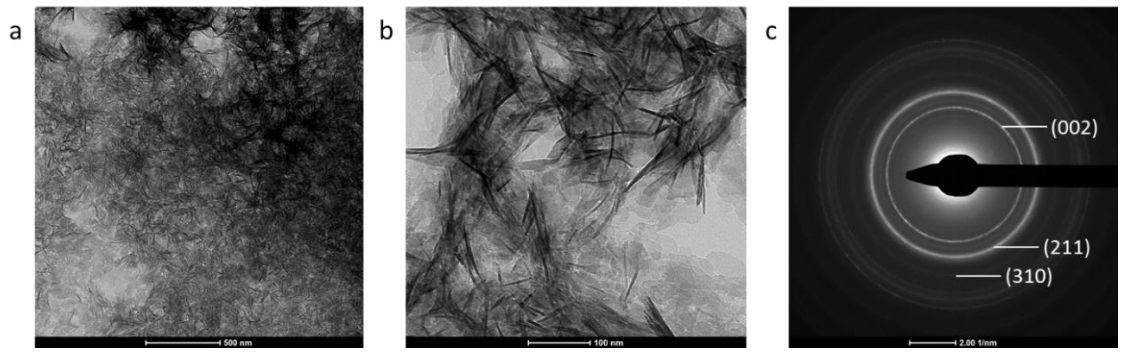

Figure 35: Control experiment with reduced pAsp to enhance CaP formation. a) high density presence of crystal structures. b) plate-like structures in agreement with literature and experiment 3. c) Diffraction pattern clearly indicating CaP structures being present. [55]

3.5 Conclusions

In conclusion, visualizing collagen in liquid via LP-TEM, although still in an early experimental phase, appears to be feasible but requires further optimization of the parameters such as contrast and thickness, and potentially might need a different cell design. Sample thickness from top-down sample preparation has been optimized and semi-monodispersed single fibrils are obtained. SciTEM has been introduced in order to achieve the precise ultra-low liquid volume loading providing thin liquid layers.

Based on the various bulk-solution experiments, it is found that 5 g/L collagen concentration is the best condition for CaP mineralization. Future optimization of the mineral concentrations in combination with a 2 g/L collagen concentration is required to use the lab experiments to guide the liquid phase experiments.

Chapter 4 Conclusion and outlook

Collagen is the most abundant protein in bone and tissue and plays a paramount role in many structural components of the human body. Collagen fibrils are an intermediate building block in the hierarchical structure with a specific quasi-hexagonal pattern. An important feature of this pattern is D-band spacing which is attributed to a periodic occurrence of overlap and gap zone between adjacent molecules. Obtaining nanoscale information regarding both local D-band spacing changes and collagen mineralization requires state of the art analytical techniques.

This thesis demonstrates that *in-situ* TEM is a powerful analytical tool in analyzing collagen fibril deformation mechanisms at nanoscale. Additional support for inhomogeneous mechanical behavior of collagen is provided while demonstrating that biological materials can be visualized for long periods of time without being damaged. A future step for collagen deformation will be imaging in native conditions which requires further development of low dose LP-TEM imaging protocols. Additionally, development of tailored *in-situ* TEM holders which enable visualization of mechanical effects on materials will contribute significantly to material science advancement in the field.

In this work considerable steps have been made towards monitoring the mineralization behavior of collagen *in-situ*. Sample preparation and liquid dosing protocols have been established. Challenges regarding contrast and thickness have been addressed and potential solutions to overcome them have been investigated. Towards future development, to enable visualization of collagen structure at relative high resolution, suggestions to develop novel liquid cell holders or the use of graphene liquid cells are made. Bottom-up assembly of collagen fibrils is identified as a potential option to obtain highly dispersed single fibrils in an ultra-thin liquid. In addition, the introduction of a tailored liquid flow LP-TEM holder with heating capabilities might enable capturing collagen mineral interactions in the early mineralization stages.

Chapter 5 Acknowledgements

My 6-year journey of acquiring a MSc degree while maintaining a full-time position at SABIC has drawn to an end and I would like to thank all the people from SMG/SPC that have assisted me during this final stage of my education. Especially, I want to thank my supervisor Hanglong, we spent many long days in the TEM lab trying to get a good vacuum in the liquid cell, seldom have I experienced such levels of frustration for something so small. Furthermore, Bert for taking over my project as supervising professor and the many fruitful discussion we had regarding my results. I cannot forget to mention my fellow MSc graduates that shared the room with me. Finally, I would like to sincerely thank my family and most importantly my wife, Linda, for supporting and believing in me all this time, I know I have been very annoying at times.

Appendix

Appendix 1: Local segment change

	Segment 1	Segment 2	Segment 3	Segment 4	Segment 5	Segment 6	Average
D-band spacing frame 10 [nm]	67.1	67.5	64.8	70.2	67.5	64.8	67.0
D-band spacing frame 332 [nm]	72.9	74.5	72.9	72.9	71.3	71.3	72.6
D-band spacing increase [nm]	5.8	7.0	8.1	2.7	3.8	6.5	5.6
D-band spacing increase [%]	8.6	10.4	**12.5**	**3.8**	5.6	10.0	8.5

Appendix 2: Collagen mineralization

The first experiment is performed using the volumes and concentrations indicated in the table below. HEPES, $CaCl_2$, and K_2HPO_4 are added to the pAsp and collagen or pAsp and milli-Q water. These suspensions are transferred to a water bath of 37 °C. Samples are taken on the third, fourth and fifth day to assess the progress of the mineralization using TEM.

Table 2: Mineralization experiment 1.

Suspension I	**Suspension II (control)**
0.5 mL supernatant collagen [2 g/L]	0.5 mL milli-Q water
0.5 mL pAsp [150 mg/L]	0.5 mL pAsp [150 mg/L]
10 µL HEPES [1 M]	10 µL HEPES [1 M]
4.5 µL $CaCl_2$ [1 M]	4.5 µL $CaCl_2$ [1 M]
10 µL K_2HPO_4 [1 M]	10 µL K_2HPO_4 [1 M]

After three days a sample is taken and deposited on a TEM grid. First indications display the presence of material around and in the fibril, which is further enhanced on day four. Unfortunately, Selected Area Electron Diffraction (SAED), in short electron diffraction (ED), confirms the absence of crystallinity confirming that no calcium-phosphate crystals have been formed. The fifth day sample shows more pronunciation of the band structure but not the crystalline structures as described by for instance Nudelman *et al.* [48]. Furthermore, bacteria like structures seem to be present in this sample.

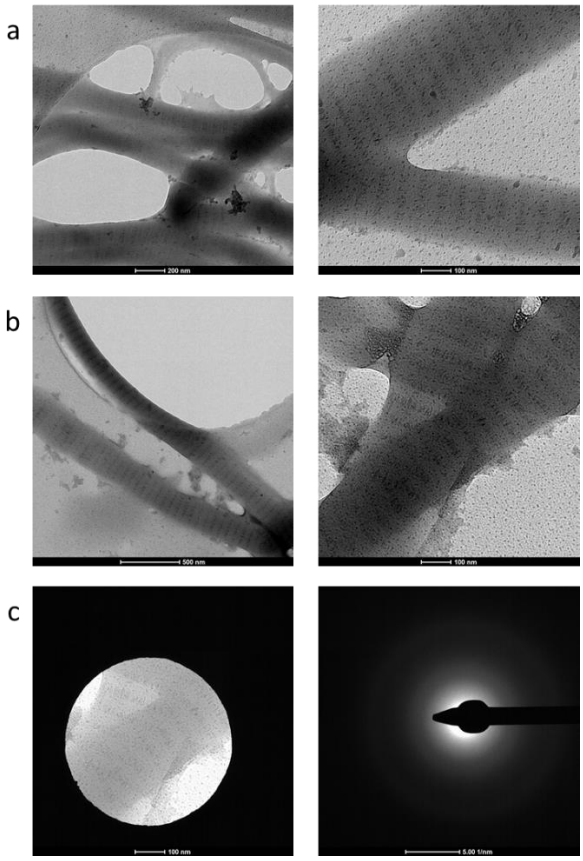

Figure 36: Potential CaP infiltration on day 3 (a) and day 4 (b), electron diffraction (c) indicates no crystallinity.

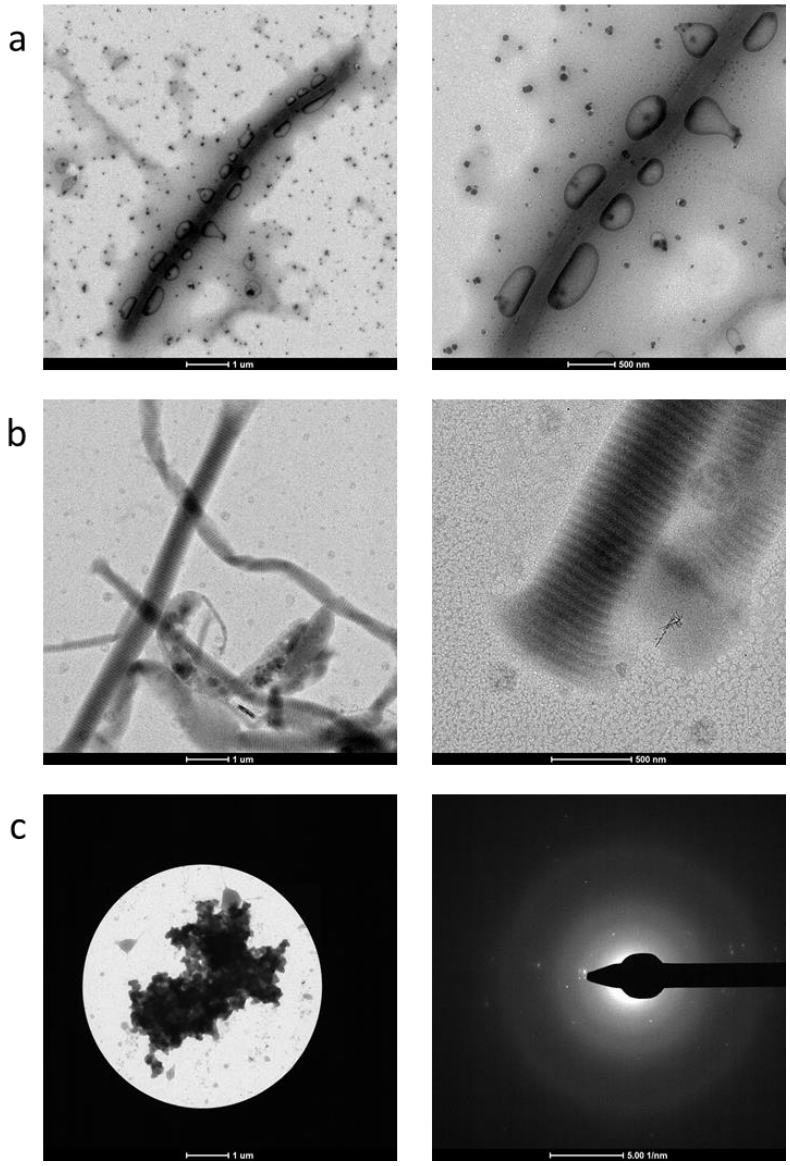

Figure 37: Day 5, appearance of bacteria like structures (a) and no visible change in banding pattern (b). c) Electron diffraction of material in control experiment indicate no significant crystalline presence.

Based on the primary results several items required optimization. HEPES and pAsp are dissolved and the pH is tuned to 7.4 using 1.0 M sodium hydroxide (Sigma). In the previous experiment the pH is not tuned, and it turned out to be slightly acidic, this could in turn affect both the collagen structure as well as the mineralization mechanism. The remaining minerals and collagen will be added to the HEPES pAsp solution. Additionally, the heating method will be a comparison between water bath and oven. The table below describes the details of the second experiment. A stock solution (solution α) is made of 25 mL milli-Q water with 59.7 mg HEPES and 1.9 mg pAsp, this solution is tuned to pH 7.4.

Table 3: Mineralization experiment 2. Suspensions II and IV serve as control experiments.

Suspension I	**Suspension II**	**Suspension III**	**Suspension IV**
3 mL solution α	3 mL solution α	3 mL solution α	3 mL solution α
6.1 mg collagen	-	5.9 mg collagen	-
13.5 µL $CaCl_2$ [1 M]	13.5 µL $CaCl_2$ [1 M]	13.5 µL $CaCl_2$ [1 M]	13.5 µL $CaCl_2$ [1 M]
6.3 µL K_2HPO_4 [1 M]	6.3 µL K_2HPO_4 [1 M]	6.3 µL K_2HPO_4 [1 M]	6.3 µL K_2HPO_4 [1 M]
Water bath	Water bath	Oven	Oven

After four days a 500 µL sample is taken from each suspension, this sample is centrifuged for 6 min at 5000 rpm followed by the removal of the supernatant. Last ethanol is added to remove excess salts, the sample is centrifuged again, and the supernatant is removed. Numerous structures are present around the fibrils in both the water bath and oven sample, unfortunately no structures present inside the fibril. These results are supported by the electron diffraction images from the two control samples. Nevertheless, the control experiments display pre-nucleation structures similar to the work of Nudelman *et al.* and Habraken *et al.* [60]

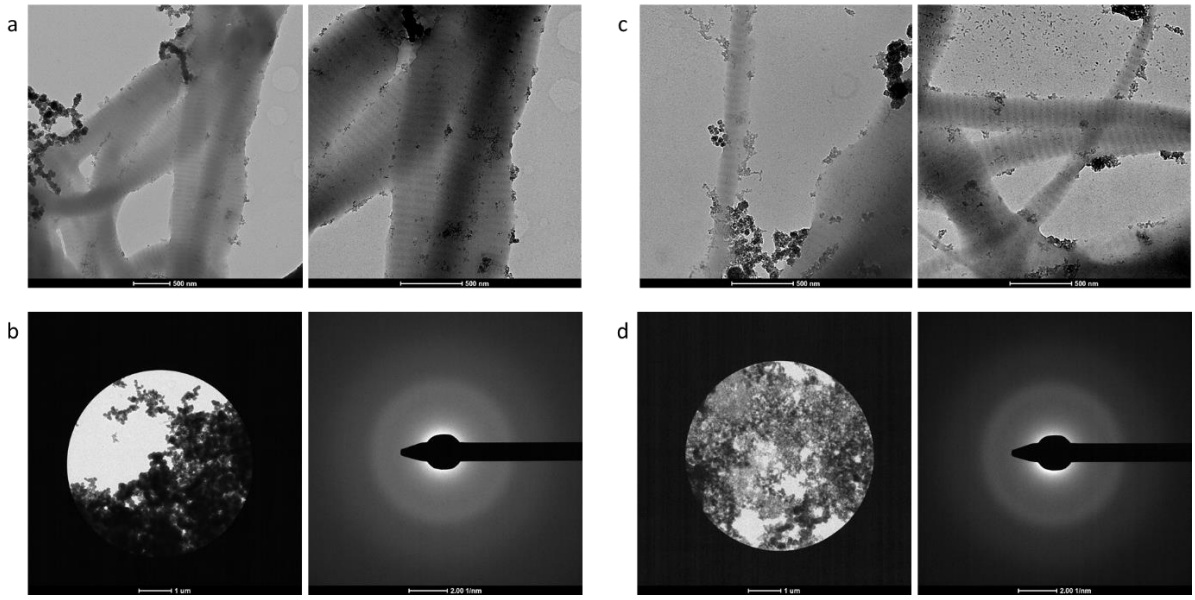

Figure 38: Day 4, minerals around collagen fibrils for both water bath (a) and oven sample (c). Electron diffraction from the water bath (b) and oven control sample (d).

At the seventh day additional samples are taken from the oven suspensions. The samples are treated identical to described above. Surrounding the fibril are equivalent structures as seen at day four, however, in the bulk solution two new features appear. Large structures resembling the amorphous calcium phosphate as visualized by Habraken *et al.* [60] and needle like structures that appear to be in line with the work of Fijneman [55]. These structures are more evident in the control sample.

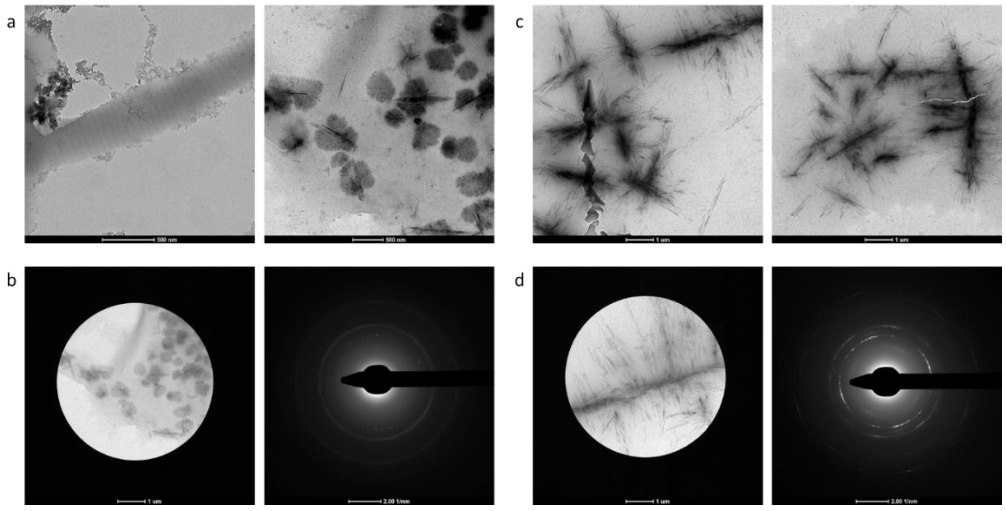

Figure 39: Day 7, structures present around fibril and in the bulk suspension (a). b) Electron diffraction from bulk structures displaying presence of crystalline phenomena. c) control sample structures and the electron diffraction (d).

The final experiment involves some minor changes to the addition order of the components, changes in the collagen concentration, and the use of an oil bath. For this experiment multiple stock solutions are made. First, solution α, 124.3 mg of HEPES dissolved in 50 mL milli-Q water and pH tuned to 7.4. Second, two 10 mL portions of solution α are taken and named α_{150} and α_{50} to which 1.5 and 0.5 mg of pAsp are added respectively. Last, solution β, 15 mL of solution α is taken and 63 µL 1.0 M K_2HPO_4 is added.

Table 4: Mineralization experiment 3.

Suspension I	**Suspension II**	**Suspension III**	**Suspension IV**
1.5 mL solution α_{150}	1.5 mL solution α_{150}	1.5 mL solution α_{50}	1.5 mL solution α_{50}
1.5 mL solution β	1.5 mL solution β	1.5 mL solution β	1.5 mL solution β
15 mg collagen	15 mg collagen	15 mg collagen	3 mg collagen supernatant
13.5 µL $CaCl_2$ [1 M]	13.5 µL $CaCl_2$ [1 M]	13.5 µL $CaCl_2$ [1 M]	13.5 µL $CaCl_2$ [1 M]
Oil	Oven	Oven	Oven

Samples are taken at the fifth day and pre-treated in the same fashion as mentioned earlier. In the case of suspension I and II results are very close to the work of Nudelman *et al.* [48] with plate-like structures being present in the fibrils together with indications of swelling. The oil bath appears to deliver the best results. Suspension III and IV indicate increased crystallization outside the fibril partly as expected since pAsp is a known crystallization inhibitor for the CaP. Electron diffraction images support this increased presence of crystalline structures. Please note that the liquid cell cannot undergo oil bath treatment, therefore direct mineralization using this approach is not possible.

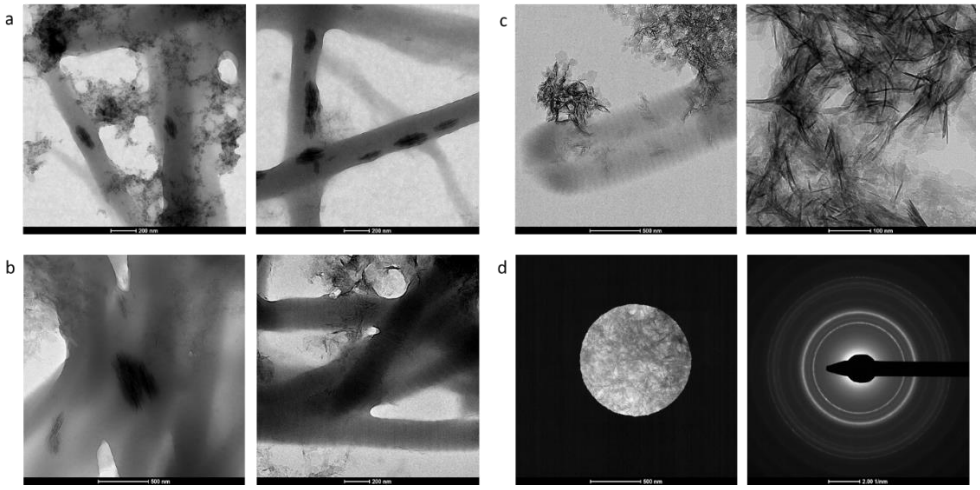

Figure 40: a) Oil bath sample with plate-like structures and fibril swelling. b) Oven sample with similar structures as oil but less obvious. c) Reduced collagen and pAsp concentration leading to crystallization outside the fibril. d) Electron diffraction from the crystal structures.

Appendix 3: sciTEM workflow

Dry TEM.run
HeadCameraLight_ON
FindTEM_Grid
BeginLoop
TakeProbe
SpotProbeRun
WashFlushMedium
scanFieldsonly
EndLoop
QC
HeadCameraLight_OFF
MoveHome

LPEM.run
HeadCameraLight_ON
FindTEM_Grid
FSRP
HeadCameraLight_OFF
LCPick
BeginLoop
TakeProbe
MoveToCameraStation
Wait2sec
PreSpot250drops
AutoDropDetection
SpotProbeRUN
HeadCameraLight_ON
QC
EndLoop
LCPlace
QC
WashFlushMedium
HeadCameraLight_OFF

References

1. Inkson BJ. Scanning electron microscopy (SEM) and transmission electron microscopy (TEM) for materials characterization. *Mater Charact Using Nondestruct Eval Methods*. January 2016:17-43. doi:10.1016/B978-0-08-100040-3.00002-X

2. Van Huis MA, Friedrich H. Electron microscopy techniques. *Nanoparticles Work Nanosci*. 2014;9783662448:191-221. doi:10.1007/978-3-662-44823-6_7

3. Williams DB, Carter CB. *Transmission Electron Microscopy - A Textbook for Materials Science*. Springer US; 2009.

4. Taheri ML, Stach EA, Arslan I, et al. Current status and future directions for in situ transmission electron microscopy. *Ultramicroscopy*. 2016;170:86-95. doi:10.1016/j.ultramic.2016.08.007

5. Ross FM. Opportunities and challenges in liquid cell electron microscopy. *Science (80-)*. 2015;350(6267). doi:10.1126/science.aaa9886

6. Tromp RM and Ross FM. ADVANCES IN In SITU ULTRA-HIGH VACUUM. *Annu Rev Mater Sci*. 2000;30:431-449.

7. de Jonge N, Ross FM. Electron microscopy of specimens in liquid. 2011. doi:10.1038/NNANO.2011.161

8. Cho H. The Use of Liquid Phase Transmission Electron Microscopy for Quantifying Interactions Between Colloidal Nanoparticles and Visualizing Their Self-Assembled Structures. 2018.

9. Ross FM. Liquid Cell Electron Microscopy. *Cambridge Univ Press*. 2016. doi:10.1017/9781316337455

10. Smeets P, Cho K, Kempen R, Sommerdijk N, De Yoreo J. Calcium carbonate nucleation driven by ion binding in a biomimetic matrix revealed by in situ electron microscopy. 2015:26. doi:10.1038/NMAT4193

11. De Yoreo JJ, Sommerdijk NAJM. Investigating materials formation with liquid-phase and cryogenic TEM. *Nat Rev Matter*. 2016:16035. doi:10.1038/natrevmats.2016.35

12. Proetto MT, Rush AM, Chien MP, et al. Dynamics of soft nanomaterials captured by transmission electron microscopy in liquid water. *J Am Chem Soc*. 2014;136(4):1162-1165. doi:10.1021/ja408513m

13. Ianiro A, Wu H, van Rijt MMJ, et al. Liquid-liquid phase separation during amphiphilic self-assembly. *Nat Chem*. 2019;11:320-328. doi:10.1038/s41557-019-0210-4

14. Patterson JP, Abellan P, Denny MS, et al. Observing the Growth of Metal–Organic Frameworks by in Situ Liquid Cell Transmission Electron Microscopy. *J Am Chem Soc*. 2015;137:7322-7328. doi:10.1021/jacs.5b00817

15. Williamson MJ, Tromp RM, Vereecken PM, Hull R, Ross FM. Dynamic microscopy of nanoscale cluster growth at the solid-liquid interface. 2003. doi:10.1038/nmat944

16. Egerton RF, Malac M. EELS in the TEM. *J Electron Spectros Relat Phenomena*. 2005;143(2-3 SPEC. ISS.):43-50. doi:10.1016/j.elspec.2003.12.009

17. Shindo D, Oikawa T. *Analytical Electron Microscopy for Materials Science*. Springer Japan; 2002. doi:10.1007/978-4-431-66988-3

18. Oikawa T. Energy dispersive X-ray spectroscopy. *Japanese J Tribol*. 2006;51(1):33-38. doi:10.1007/978-4-431-66988-3_4

19. Cho H, Jones MR, Nguyen SC, Hauwiller MR, Zettl A, Alivisatos AP. The Use of Graphene and Its Derivatives for Liquid-Phase Transmission Electron Microscopy of Radiation-Sensitive Specimens. 2016. doi:10.1021/acs.nanolett.6b04383

20. Gautieri A, Vesentini S, Redaelli A, Buehler MJ. Hierarchical structure and nanomechanics of collagen microfibrils from the atomistic scale up. *Nano Lett*. 2011;11(2):757-766. doi:10.1021/nl103943u

21. Petruska JA, Hodge AJ. A subunit model for the tropocollagen macromolecule. *Proc Natl Acad Sci United States*. 1964;51:871-876. doi:10.1073/pnas.51.5.871

22. Orgel JP, Irving TC, Miller A, Wess TJ. *Microfibrillar Structure of Type I Collagen in Situ*. Vol 13.; 2006. www.pnas.orgcgidoi10.1073pnas.0502718103. Accessed October 15, 2019.

23. Piez KA, Trus BL. Sequence regularities and packing of collagen molecules. *J Mol Biol*. 1978;122(4):419-432. doi:10.1016/0022-2836(78)90419-9

24. Chapman JA, Tzaphlidou M, Meek KM, Kadler KE. The collagen fibril-A model system for studying the staining and fixation of a protein. *Electron Microsc Rev*. 1990;3(1):143-182. doi:10.1016/0892-0354(90)90018-N

25. Doyle BB, Hukins DWL, Hulmes DJS, Miller A, Rattew CJ, Woodhead-Galloway J. Origins and implications of the D stagger in collagen. *Biochem Biophys Res Commun*. 1974;60(2):858-864. doi:10.1016/0006-291X(74)90320-9

26. Zhu J, Hoop CL, Case DA, Baum J. Cryptic binding sites become accessible through surface reconstruction of the type I collagen fibril. *Sci REPORtS |*. 2018;8:16646. doi:10.1038/s41598-018-34616-z

27. Wallace JM, Chen Q, Fang M, Erickson B, Orr BG, Banaszak Holl MM. Type i collagen exists as a distribution of nanoscale morphologies in teeth, bones, and tendons. *Langmuir*. 2010;26(10):7349-7354. doi:10.1021/la100006a

28. Folkhard W, Mosler E, Geercken W, et al. Quantitative analysis of the molecular sliding mechanisms in native tendon collagen - time-resolved dynamic studies using synchrotron radiation. *Int J Biol Macromol*. 1987. doi:10.1016/0141-8130(87)90047-X

29. Fratzl P, Misof K, Zizak I, Rapp G, Amenitisch H, Bernstorff S. Fibrillar Structure and Mechanical Properties of Collagen. *J Struct Biol*. 1997;122:119-122.

30. Gautieri A, Vesentini S, Redaelli A, Buehler MJ. Viscoelastic properties of model segments of collagen molecules. *Matrix Biol*. 2012;31(2):141-149. doi:10.1016/J.MATBIO.2011.11.005

31. Liu Y, Ballarini R, Eppell SJ. Tension tests on mammalian collagen fibrils. *Interface Focus*. 2016;6(1). doi:10.1098/rsfs.2015.0080

32. Peacock CJ, Kreplak L. Nanomechanical mapping of single collagen fibrils under tension †. *Nanoscale*. 2019;11. doi:10.1039/c9nr02644d

33. Redaelli A, Vesentini S, Soncini M, Vena P, Mantero S, Montevecchi FM. Possible role of decorin glycosaminoglycans in fibril to fibril force transfer in relative mature tendons—a computational study from molecular to microstructural level. *J Biomech*. 2003;36(10):1555-1569. doi:10.1016/S0021-9290(03)00133-7

34. Rigozzi S, Müller R, Stemmer A, Snedeker JG. Tendon glycosaminoglycan proteoglycan

sidechains promote collagen fibril sliding—AFM observations at the nanoscale. *J Biomech*. 2013;46(4):813-818. doi:10.1016/J.JBIOMECH.2012.11.017

35. Sasaki N, Odajima S. Elongation mechanism of collagen fibrils and force-strain relations of tendon at each level of structural hierarchy. *J Biomech*. 1996;29(9):1131-1136. doi:10.1016/0021-9290(96)00024-3

36. Shen ZL, Dodge MR, Kahn H, Ballarini R, Eppell SJ. Stress-strain experiments on individual collagen fibrils. *Biophys J*. 2008;95(8):3956-3963. doi:10.1529/biophysj.107.124602

37. Tang Y, Ballarini R, Buehler MJ, Eppell SJ. Deformation micromechanisms of collagen fibrils under uniaxial tension. *J R Soc Interface*. 2010;7(46):839-850. doi:10.1098/rsif.2009.0390

38. van der Rijt JAJ, van der Werf KO, Bennink ML, Dijkstra PJ, Feijen J. Micromechanical testing of individual collagen fibrils. *Macromol Biosci*. 2006;6(9):699-702. doi:10.1002/mabi.200600063

39. Wells HC, Sizeland KH, Kayed HR, et al. Poisson's ratio of collagen fibrils measured by small angle X-ray scattering of strained bovine pericardium. *J Appl Phys*. 2015;117:44701. doi:10.1063/1.4906325

40. van der Rijt JAJ. Mircomechanical testing of single collagen type i fibrils. PhD thesis, University of Twente, Enschede, The Netherlands, 2004.

41. Puxkandl R, Zizak I, Paris O, et al. Viscoelastic properties of collagen: Synchrotron radiation investigations and structural model. *Phil Trans R Soc B Biol Sci*. 2002;357(1418):191-197. doi:10.1098/rstb.2001.1033

42. Buehler MJ. Nature designs tough collagen: Explaining the nanostructure of collagen fibrils. *Proc Natl Acad Sci*. 2006;103(33):12285-12290. doi:10.1073/pnas.0603216103

43. Gautieri A, Passini FS, Silván U, et al. Advanced glycation end-products: Mechanics of aged collagen from molecule to tissue. *Matrix Biol*. 2017;59:95-108. doi:10.1016/J.MATBIO.2016.09.001

44. Gutsmann T, Fantner GE, Venturoni M, et al. Evidence that Collagen Fibrils in Tendons Are Inhomogeneously Structured in a Tubelike Manner. *Biophys J*. 2003;84(4):2593-2598. doi:10.1016/S0006-3495(03)75064-4

45. Thompson RF, Walker M, Siebert CA, Muench SP, Ranson NA. An introduction to sample preparation and imaging by cryo-electron microscopy for structural biology. *Methods*. 2016. doi:10.1016/j.ymeth.2016.02.017

46. Barreto-Vieira DF, Barth OM. Negative and Positive Staining in Transmission Electron Microscopy for Virus Diagnosis. *Microbiol Agric Hum Heal*. 2015. doi:10.5772/60511

47. Kim D, Lee B, Thomopoulos S, Jun YS. The role of confined collagen geometry in decreasing nucleation energy barriers to intrafibrillar mineralization. *Nat Commun*. 2018;9(1). doi:10.1038/s41467-018-03041-1

48. Nudelman F, Pieterse K, George A, et al. The role of collagen in bone apatite formation in the presence of hydroxyapatite nucleation inhibitors. *Nat Mater*. 2010;9(12):1004-1009. doi:10.1038/nmat2875

49. Xu Z, Zhao W, Wang Z, Yang Y, Sahai N. Structure analysis of collagen fibril at atomic-level resolution and its implications for intra-fibrillar transport in bone biomineralization. *Phys Chem Chem Phys*. 2018;20(3):1513-1523. doi:10.1039/c7cp05261h

50. Olszta MJ, Cheng X, Jee SS, et al. Bone structure and formation: A new perspective. *Mater Sci Eng R Reports*. 2007;58(3-5):77-116. doi:10.1016/j.mser.2007.05.001

51. Cheng A, Henderson R, Mastronarde D, et al. MRC2014: Extensions to the MRC format header for electron cryo-microscopy and tomography. *J Struct Biol*. 2015;192(2):146-150. doi:10.1016/j.jsb.2015.04.002

52. Silver FH, Christiansen DL, Snowhill PB, Chen Y. Transition from viscous to elastic-based dependency of mechanical properties of self-assembled type I collagen fibers. *J Appl Polym Sci*. 2001;79(1):134-142. doi:10.1002/1097-4628(20010103)79:1<134::AID-APP160>3.0.CO;2-E

53. Erickson B, Fang M, Wallace JM, Orr BG, Les CM, Banaszak Holl MM. Nanoscale Structure of Type I Collagen Fibrils: Quantitative Measurement of D-spacing. *Biotechnol J*. 2013;8(1):117-126. doi:10.1002/biot.201200174

54. Niu LN, Jee SE, Jiao K, et al. Collagen intrafibrillar mineralization as a result of the balance between osmotic equilibrium and electroneutrality. *Nat Mater*. 2017;16(3):370-378. doi:10.1038/nmat4789

55. Fijneman AJ. Studying collagen mineralization with advanced microscopic techniques. MSc thesis, University of Eindhoven, Department of Chemical Engineering and Chemistry, *2016.*

56. Patterson JP, Parent LR, Cantlon J, et al. Picoliter Drop-On-Demand Dispensing for Multiplex Liquid Cell Transmission Electron Microscopy. 2016;1(8). doi:10.1017/S1431927616000659

57. Tannenberg R, Eickhoff H, Weigel W. *Imaging Nanoparticle Arrays Loading Method for Multiplexing Nanoparticle Characterization*. www.imaging-git.com. Accessed January 6, 2020.

58. Touve MA, Figg CA, Wright DB, et al. Polymerization-Induced Self-Assembly of Micelles Observed by Liquid Cell Transmission Electron Microscopy. doi:10.1021/acscentsci.8b00148

59. Moser TH, Mehta H, Park C, Kelly RT, Shokuhfar T, Evans JE. The role of electron irradiation history in liquid cell transmission electron microscopy. *Sci Adv*. 2018;4(4). doi:10.1126/sciadv.aaq1202

60. Habraken W, Habibovic P, Epple M, Bohner M. Calcium phosphates in biomedical applications: Materials for the future? *Mater Today*. 2016;19(2):69-87. doi:10.1016/j.mattod.2015.10.008